The Astrophysical Journal, 977:15 (27pp), 2024 December 10 https://doi.org/10.3847/1538-4357/ad856c

Rotation at the Fully Convective Boundary: Insights from Wide WD + MS Binary Systems

Federica Chiti[1], Jennifer L. van Saders[1], Tyler M. Heintz[2], J. J. Hermes[2], J. M. Joel Ong (王加冕)[1,4], Daniel R. Hey[1], Michele M. Ramirez-Weinhouse[3], and Alison Dugas[1]
[1] Institute for Astronomy, University of Hawaiʻi at Mānoa, 2680 Woodlawn Dr., Honolulu, HI 96822, USA
[2] Department of Astronomy & Institute for Astrophysical Research, Boston University, 725 Commonwealth Ave., Boston, MA 02215, USA
[3] Lānaʻi High and Elementary School, 555 Fraser Ave., Lanai City, HI 96763, USA
Received 2024 March 16; revised 2024 September 15; accepted 2024 October 2; published 2024 November 28

Abstract

Gyrochronology, a valuable tool for determining ages of low-mass stars where other techniques fail, relies on accurate calibration. We present a sample of 185 wide (>100 au) white dwarf + main sequence (WD + MS) binaries. Total ages of WDs are computed using all-sky survey photometry, Gaia parallaxes, and WD atmosphere models. Using a magnetic braking law calibrated against open clusters, along with assumptions about initial conditions and angular momentum transport, we construct gyrochrones to predict the rotation periods of MS stars. Both data and models show that, at the fully convective boundary (FCB), MS stars with WD ages of up to 7.5 Gyr and within a <50 K effective temperature range experience up to a threefold increase in rotation period relative to stars slightly cooler than the FCB. We suggest that rapid braking at this boundary is driven by a sharp rise in the convective overturn timescale (τ_{cz}) caused by structural changes between partially and fully convective stars and the ^{3}He instability occurring at this boundary. While the specific location in mass (or temperature) of this feature varies with model physics, we argue that its existence remains consistent. Stars along this feature exhibit rotation periods that can be mapped, within 1σ, to a range of gyrochrones spanning ≈6 Gyr. Due to current temperature errors (≃50 K), this implies that a measured rotation period cannot be uniquely associated to a single gyrochrone, implying that gyrochronology may not be feasible for M dwarfs very close to the FCB.

Unified Astronomy Thesaurus concepts: Stellar rotation (1629); Stellar ages (1581); Stellar activity (1580); Stellar magnetic fields (1610); Stellar evolution (1599); White dwarf stars (1799)

Materials only available in the online version of record: machine-readable tables

1. Introduction

Ages of stars are critical to our understanding of the evolution of astrophysical systems and yet are one of the most difficult stellar properties to measure. The only star for which we have a precise and accurate age is the Sun; for any other star, age can only be estimated or inferred. There are many techniques to estimate stellar ages, but there is no single method that is applicable to all spectral types (D. R. Soderblom 2010).

K and M dwarfs are the most numerous stars in the Galaxy and have lifetimes longer than the age of the Milky Way disk, meaning that they preserve a record of the history of star formation and chemical evolution of the Galaxy. They are, however, resistant to standard age-dating techniques. Isochrone fitting fails to provide constraints on stellar ages when used on low-mass stars, due to their slow nuclear evolution (Y. Takeda et al. 2017). Similarly, asteroseismology, which provides precise ages for Sun-like stars, cannot be used to date low-mass stars like K and M dwarfs due to their low oscillation amplitudes (W. J. Chaplin et al. 2011).

A promising tool in this low-mass regime is gyrochronology (S. A. Barnes 2007), which derives ages for cool main-sequence (MS) stars by exploiting the fact that they spin down with time (A. Skumanich 1972) due to magnetic braking. Magnetic braking is the mechanism by which a star loses angular momentum to magnetized stellar winds over time as the result of the interaction between mass loss and dynamo-driven stellar magnetic fields. C. R. Epstein & M. H. Pinsonneault (2014) showed that under Skumanich-type spindown, rotation-based age dating is potentially among the most precise methods available.

Calibration of period–age relations for low-mass stars requires a large sample of old, well-dated low-mass stars. However, only a handful of stars below 0.8 $M_\odot$ are currently available, and most of them are in young clusters (4 Gyr at the oldest; R. Dungee et al. 2022). Furthermore, observations of these clusters have shown that standard braking models fail to reproduce the observed rotational sequences, suggesting that stellar spindown may not be as simple as it once appeared.

Recent measurements of the rotation period (P_{rot}) of stars in the benchmark open clusters Praesepe (≈700 Myr; S. T. Douglas et al. 2019) and NGC 6811 (1 Gyr; S. Meibom et al. 2011; K. Janes et al. 2013) show that a simple power law with a braking index n ($n = 0.5$ in the Skumanich law) fails at predicting the observed rotational sequences in these clusters (J. L. Curtis et al. 2020). While solar-type stars in NGC 6811 have longer periods compared to their counterparts in the younger cluster Praesepe, the two sequences merge at $M < 0.8\,M_\odot$ (K0- to M0-type stars; J. L. Curtis et al. 2019; S. T. Douglas et al. 2019). In other words, the spindown

[4] NASA Hubble Fellow.

appears to "stall" (or reduce) for low-mass stars in NGC 6811. F. Spada & A. C. Lanzafame (2020) demonstrated that this phenomenon can be explained by relaxing the assumption of solid-body rotation and allowing for angular momentum (AM) transport between the core and the envelope (i.e., radial differential rotation). The spindown stalling observed in K- and early-M-type stars in NGC 6811 is putatively an epoch when AM transport from the core to the envelope balances the AM loss at the surface due to winds. The lack of a radiative core in fully convective stars that can support such core-envelope interaction may be responsible for the closure of the intermediate period gap discovered with Kepler by A. McQuillan et al. (2013) at the fully convective boundary (FCB; Y. L. Lu et al. 2021).

Near the FCB, another relevant feature is the underdensity of stars observed near $M_G = 10.2$ in the main sequence on the Hertzsprung–Russell diagram found by W.-C. Jao et al. (2018) using Gaia DR2 measurements. It has been proposed that this Gaia M-dwarf gap is a manifestation of the location where stars transition from partially to fully convective, which is predicted to occur at a mass of $\sim 0.35\,M_{\odot}$. Earlier theoretical work by J. L. van Saders & M. H. Pinsonneault (2012a) demonstrated that stars slightly above this threshold undergo a structural instability due to nonequilibrium ^{3}He burning during the first few billion years on the main sequence. This results in the development of a convective core, separated from a deep convective envelope by a thin radiative layer. The continuous accumulation of central ^{3}He causes the radiative zone separating them to thin even further, initiating fully convective episodes. Using stellar models and stellar population synthesis, G. A. Feiden et al. (2021) confirmed that the ^{3}He instability is responsible for the appearance of the M-dwarf gap.

With the distinct structural changes across the FCB, there have been attempts to comprehend whether there are any consequences for the magnetic properties, activity levels, and rotation rates of stars. For instance, J.-F. Donati et al. (2008) and A. Reiners & G. Basri (2009) demonstrated that $0.34-0.36\,M_{\odot}$ stars are prone to undergo sudden alterations in their large-scale magnetic topologies, which could lead to observable surface activity signatures. More recently, W.-C. Jao et al. (2023) conducted a high-resolution spectroscopic Hα emission survey of M dwarfs spanning the Gaia M-dwarf gap and argued that stars above the top gap edge exhibit Hα emission while stars within the gap or below do not display any emission. Thus, stars near the FCB provide a powerful laboratory for testing the physics of M-dwarf stars, including those affected by the ^{3}He instability. Moreover, having a reliable spindown model that can predict the rotational evolution of these stars is crucial for determining a precise period–age relation for old, low-mass stars.

A primary limitation is the lack of empirical anchors of known age for old K- and M-type stars. Open clusters have been the major contributors of calibrators to date; however, due to their short dissipation timescales ($\sim$200 Myr; R. Wielen 1971), old clusters are rare and tend to be more distant and challenging to observe. The standard gyrochronology calibrators and the recent observations of late-K and early-M dwarfs in M67 (R. Dungee et al. 2022) do not extend beyond 4 Gyr for stars below $0.8\,M_{\odot}$. Likewise, the asteroseismic calibrator sample that has been important for understanding braking in solar-mass stars (J. L. van Saders et al. 2016; O. J. Hall et al. 2021) does not extend below $\approx 0.8\,M_{\odot}$.

Wide binaries that contain a white-dwarf (WD) companion provide a distinctive opportunity to determine the ages of field stars. WDs are the end product of stars with initial masses of less than $8-10\,M_{\odot}$ and, as they no longer undergo nuclear fusion in their core, they gradually cool with time, becoming dimmer and colder. Because their effective temperature and mass uniquely correspond to a single cooling age (given a composition), WDs have been utilized as stellar clocks for decades (G. Fontaine et al. 2001) to date a variety of stellar populations, such as our Galaxy—see E. García-Berro & T. D. Oswalt (2016) and references therein—and open and globular clusters—see D. E. Winget et al. (2009), E. García--Berro et al. (2010), E. J. Jeffery et al. (2011), and B. M. S. Hansen et al. (2013) for some examples. The advancement of robust cooling models (P. Bergeron et al. 1995) allows WDs to serve as precise and dependable age indicators. However, to determine the complete age of a WD, one needs to consider the time from its zero-age main sequence (ZAMS) to its present state as a WD. This involves using a semiempirical initial-final mass relation (IFMR) in conjunction with stellar evolution model grids to ascertain the progenitor lifetimes from the ZAMS to the WD phase. Using photometry only, T. M. Heintz et al. (2022) found that WD ages are precise at the 25% level for WDs with masses $>0.63\,M_{\odot}$.

Wide, coeval binaries are sufficiently distant ($>$100 au) that the two stars can be expected to evolve as single stars without any interaction between them (R. J. White & A. M. Ghez 2001). Therefore, the WD companion offers an independent age estimate of the entire system, making it possible to extend period–age relationships to the age of the Galactic disk for the most common stars in our Galaxy. Previous studies have leveraged on wide WD + MS binary systems to investigate the age–metallicity–activity relation (J. K. Zhao et al. 2011), the age–velocity relation (R. Raddi et al. 2022), and the age–metallicity relation (A. Rebassa-Mansergas et al. 2016, 2021). Close WD + MS binaries have also been used to constrain the relations between magnetic activity, rotation, magnetic braking, and age in M stars (D. P. Morgan et al. 2012; A. Rebassa-Mansergas et al. 2013; J. N. Skinner et al. 2017; A. Rebassa-Mansergas et al. 2023).

The number of wide coeval binary systems has significantly increased since the launch of the Gaia spacecraft. From Gaia DR2, K. El-Badry & H.-W. Rix (2018) constructed a catalog of over $\sim$53,000 binaries, $\sim$3000 of which contained a WD and a main-sequence star, which represented a tenfold increase in the number of known coeval binaries (J. B. Holberg et al. 2013). With the release of Gaia eDR3, K. El-Badry et al. (2021) published an extensive catalog of 1.3 million spatially resolved binary stars within $\approx$1 kpc of the Sun, including more than 16,000 WD + MS binaries, which increased the sample by another order of magnitude. This increase presents an opportunity to infer precision ages for cool, old stars, which are the focus of this work.

In Section 2 we describe the physics of the rotational evolution models, their calibration, and the technique used to determine WD ages. In Section 3, we present the sample selection of WD + MS systems. The ages of these systems as revealed by our models and WDs are discussed in Section 4, where we also compare our sample to other data sets. Finally, the conclusions of our results are presented in Section 5.

2. Methods

2.1. Gyrochronology Models

We use the rotation code `rotevol` (J. L. van Saders & M. H. Pinsonneault 2013; G. Somers et al. 2017) to model the AM evolution of a star. We use as input nonrotating tracks with stellar masses between 0.18 and 1.15 $M_{\odot}$, generated using the Yale Rotating Evolution Code (`YREC`; see J. L. van Saders & M. H. Pinsonneault 2012b; M. H. Pinsonneault et al. 1989; J. N. Bahcall & M. H. Pinsonneault 1992). The models include helium and heavy element diffusion following A. A. Thoul et al. (1994), but with the diffusion coefficients multiplied by a factor of 0.753 to match the helioseismically determined helium abundance (S. Basu & H. M. Antia 1995) in the Sun at solar age. We adopt boundary conditions using the F. Allard et al. (1997) atmospheric tables and OPAL opacities (C. A. Iglesias & F. J. Rogers 1996) with low-temperature opacities from J. W. Ferguson et al. (2005) for an N. Grevesse & A. J. Sauval (1998) solar mixture. We adopt nuclear reaction rates from E. G. Adelberger et al. (2011) with weak screening (E. E. Salpeter 1954) and the equation of state from the OPAL project (F. J. Rogers et al. 1996; F. J. Rogers & A. Nayfonov 2002). We assume no overshooting, and a mixing-length theory of convection (J. P. Cox & R. T. Giuli 1968; E. Vitense 1953). Our solar-calibrated model at 4.57 Gyr (J. N. Bahcall et al. 1995) has $Z = 0.01709$, $X = 0.71642$, and mixing-length parameter $\alpha_{\rm ml} = 1.94243$. We run models at a range of surface spot covering fractions in YREC (0%, 25%, and 50%) following the prescription of G. Somers & M. H. Pinsonneault (2015) and G. Somers et al. (2020) with a spot temperature contrast ratio $x_{\rm spot} = 0.8$ but retain otherwise identical physical ingredients in the spotted models.

We run YREC in the nonrotating configuration and compute the rotational evolution post hoc using the tracer code `rotevol` (J. L. van Saders & M. H. Pinsonneault 2013; G. Somers et al. 2017). The benefit of this approach is that we can rapidly search parameter space when fitting the magnetic braking law to the observations; the downside is that rotation cannot influence the structure. While this is a reasonable assumption for all but the most rapid rotators, ideally one would actively couple the starspot filling fraction to the rotation rate (e.g., L. Cao & M. H. Pinsonneault 2022; L. Cao et al. 2023). We leave this exercise to future work, and instead examine the behavior of a range of fixed spot covering fractions.

To model the rotation-period evolution of a star as a function of time, one must choose appropriate initial starting conditions as well as specify prescriptions for three processes that drive the angular momentum (AM) evolution: early disk interactions, AM loss at the stellar surface through magnetized winds ("braking law"), and internal AM transport. In this section, we describe the ingredients and assumptions of the stellar evolutionary models.

2.1.1. Initial Conditions

The initial rotation periods of our models are taken from the observed periods distribution of the young cluster Upper Sco at 10 Myr. Upper Sco is the most populated cluster sample in the mass range of interest of this work and, by its age, massive accretion disks are nearly absent (J. P. Williams & L. A. Cieza 2011) and significant AM loss has not occurred yet (G. Somers et al. 2017; L. M. Rebull et al. 2018). Therefore, Upper Sco is representative of other young clusters and an ideal data set from which to infer initial rotational periods. We divide the Upper Sco data into mass deciles between the 10th and the 90th percentile masses and compute the median rotation period for each mass bin. The rotation periods are interpolated with respect to the midpoints of the mass bins using a 1D smoothing spline. We evaluate $P_{\rm init}$ for each stellar mass available in our model grid, as shown in Figure 1.

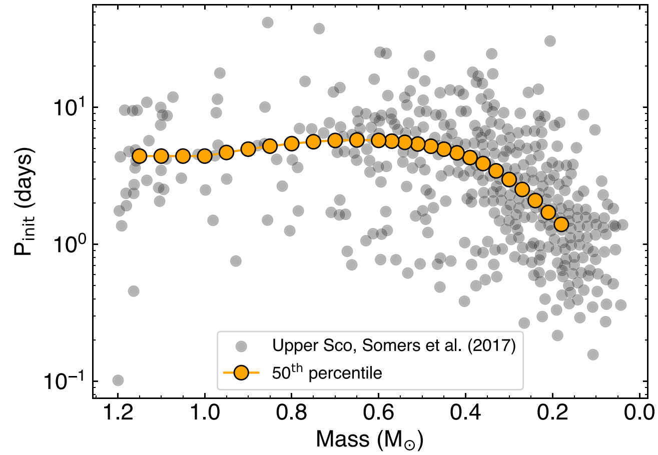

Figure 1. The Upper Sco rotation distribution at 10 Myr (G. Somers et al. 2017) from which we adopt the initial rotation periods for the model tracks. The solid yellow line shows a 1D smoothing spline fit to the median rotation periods. This fit is evaluated at the stellar masses available in our model grid to compute their respective $P_{\rm init}$.

2.1.2. Magnetic Braking

We adopt the J. L. van Saders & M. H. Pinsonneault (2013) formulation of the classic wind braking law proposed by S. D. Kawaler (1988). We assume that the magnetic field scales as

$$\frac{B}{B_{\odot}} = \left(\frac{P_{\rm phot}}{P_{\rm phot,\odot}}\right)^{0.5} \begin{cases} \dfrac{\omega_{\rm sat}}{\omega_{\odot}} & \omega_{\rm sat} \leqslant \omega\dfrac{\tau_{cz}}{\tau_{cz,\odot}} \\ \dfrac{\omega\tau_{cz}}{\omega_{\odot}\tau_{cz,\odot}} & \omega_{\rm sat} > \omega\dfrac{\tau_{cz}}{\tau_{cz,\odot}} \end{cases}, \quad (1)$$

and tie the mass-loss rate to the empirical scaling of $\dot{M}$ with X-ray luminosity from B. E. Wood et al. (2005), with X-ray luminosity given by the N. Pizzolato et al. (2003) scaling with Rossby number ($\mathrm{Ro} = P_{\rm rot}/\tau_{cz} = 2\pi/\omega\tau_{cz}$)

$$\frac{\dot{M}}{\dot{M}_{\odot}} = \left(\frac{L_{\rm bol}}{L_{\rm bol,\odot}}\right) \begin{cases} \left(\dfrac{\omega_{\rm sat}}{\omega_{\odot}}\right)^2 & \omega_{\rm sat} \leqslant \omega\dfrac{\tau_{cz}}{\tau_{cz,\odot}} \\ \left(\dfrac{\omega\tau_{cz}}{\omega_{\odot}\tau_{cz,\odot}}\right)^2 & \omega_{\rm sat} > \omega\dfrac{\tau_{cz}}{\tau_{cz,\odot}} \end{cases}. \quad (2)$$

Therefore, we parameterize the AM loss as

$$\frac{dJ}{dt} = \begin{cases} f_K K_M \omega \left(\dfrac{\omega_{\rm sat}}{\omega_{\odot}}\right)^2 & \omega_{\rm sat} \leqslant \omega\dfrac{\tau_{cz}}{\tau_{cz,\odot}} \\ f_K K_M \omega \left(\dfrac{\omega\tau_{cz}}{\omega_{\odot}\tau_{cz,\odot}}\right)^2 & \omega_{\rm sat} > \omega\dfrac{\tau_{cz}}{\tau_{cz,\odot}} \end{cases}, \quad (3)$$

where f_K is a normalization constant tuned to reproduce the observed rotation at known age; ω is the rotation rate; $\omega_\odot$ is the rotation rate of the Sun (2.86×10^{-6} rad s^{-1}); $\omega_{\rm sat}$ is the saturation threshold; τ_{cz} is the convective overturn timescale; K_M is the product

$$\frac{K_M}{K_{M,\odot}} = c(\omega)\left(\frac{R}{R_\odot}\right)^{3.1}\left(\frac{M}{M_\odot}\right)^{-0.22}\left(\frac{L}{L_\odot}\right)^{0.56}\left(\frac{P_{\rm phot}}{P_{\rm phot,\odot}}\right)^{0.44} \quad (4)$$

with luminosity L, mass M, radius R, and photospheric pressure $P_{\rm phot}$; $c(\omega)$ is the centrifugal correction from S. P. Matt et al. (2012).

We do not include weakened magnetic braking (J. L. van Saders et al. 2016), as the low-mass stars in our sample are not expected to reach the relevant Ro within the age of the Galactic disk (J. L. van Saders et al. 2019).

2.1.3. AM Redistribution

For the internal AM transport, we adopt the prescription for core-envelope coupling as described in P. A. Denissenkov et al. (2010). The basic assumption of this model, which was originally proposed by K. B. MacGregor & M. Brenner (1991) as the double-zone model, is that the core and the envelope rotate rigidly, but not necessarily at the same rate. This assumption is roughly consistent with the current rotational state of the solar interior (P. A. Denissenkov et al. 2010). The rate at which the two zones are allowed to exchange angular momentum is defined by the core-envelope coupling timescale τ_c, which is assumed to be constant along the evolution and a function of stellar mass as in F. Spada & A. C. Lanzafame (2020)

$$\tau_c = \tau_{c,\odot}\left(\frac{M_*}{M_\odot}\right)^{-\alpha} \quad (5)$$

where $\tau_{c,\odot}$ is the solar rotational coupling timescale ($\approx$22 Myr; F. Spada & A. C. Lanzafame 2020) and α is a power-law exponent of this mass-dependent timescale for transport. This scaling was found to remain consistent regardless of the choice of wind braking law and in good agreement with the separate analysis of core-envelope re-coupling by G. Somers & M. H. Pinsonneault (2016). A. C. Lanzafame & F. Spada (2015) found $\alpha = 7.28$, and F. Spada & A. C. Lanzafame (2020) refined this estimate to $\alpha = 5.6$ using new data of the clusters Praesepe and NGC 6811 that extended to lower-mass stars. More recently, L. Cao et al. (2023) found $\alpha = 11.8$ by using spotted models to fit the rotational sequences in the Pleiades and Praesepe. We leave it as a free parameter in our calibration fits.

Thus, our model has five parameters, of which two are set as follows: $P_{\rm init}$ is given by the Upper Sco rotational distribution at 10 Myr shown in Figure 1; the solar rotational coupling timescale is fixed at 22 Myr. We fit for the remaining three parameters: the normalization constant f_K and the saturation threshold $\omega_{\rm sat}$ in the braking law, and the exponent α in the core-envelope coupling timescale mass dependence.

2.1.4. Model Calibration

To constrain f_K, $\omega_{\rm sat}$, and α, we calibrate the models such that they can reproduce the rotational distributions in the Pleiades (120 Myr; L. M. Rebull et al. 2016), Praesepe (670 Myr; S. T. Douglas et al. 2017, 2019), NGC 6811 (1 Gyr; J. L. Curtis et al. 2019), NGC 6819 (2.5 Gyr; S. Meibom et al. 2015), Ruprecht 147 (2.7 Gyr; J. L. Curtis et al. 2020), and M67 (4.0 Gyr; R. Dungee et al. 2022).

For each cluster, we identify the stars suitable for model fitting by selecting those that have converged onto the slowly rotating sequence. To achieve this, we first divide the data into temperature bins and calculate the standard deviation of the rotation periods in each bin, $\sigma_{P_{\rm rot}}$. Bins with low $\sigma_{P_{\rm rot}}$ are retained, as they contain stars that have converged onto the cluster's slowly rotating sequence. By contrast, bins with high $\sigma_{P_{\rm rot}}$ are discarded, as they represent stars that have not yet converged. For the Pleiades, stars with $P_{\rm rot} < 2$ days are excluded from this analysis, as they belong to the fast rotating sequence. We generally use a temperature bin width of 300 K, except for Praesepe, which has the largest number of stars and thus requires finer binning, with a width of 100 K. Each cluster is visually inspected to determine the value of $\sigma_{P_{\rm rot}}$ that maximizes the number of stars converged onto the slowly rotating sequence. For the Pleiades, the youngest cluster, where $P_{\rm rot}$ shows the greatest scatter, we set $\sigma_{P_{\rm rot}} = 1$ day. For M67, the oldest cluster, we set $\sigma_{P_{\rm rot}} = 5$ days. For the remaining clusters, $\sigma_{P_{\rm rot}} = 3$ days. This method allows us to avoid imposing a fixed initial rotation period on stars that have not yet converged and continue to exhibit variability in their rotation periods. Note that while stars in Praesepe and NGC 6811 hotter than 6000 K and 6200K, respectively, have converged onto the clusters' slowly rotating sequences, we exclude such stars from model calibration as we lack model tracks with [Fe/H] = +0.2 and solar metallicity with effective temperatures higher than these values.

We initialize non-spotted ($f_{\rm spot} = 0\%$) tracks with masses between 0.18 $M_\odot$ and 0.65 $M_\odot$ with a 0.03 $M_\odot$ step and between 0.65 $M_\odot$ and 1.15 $M_\odot$ with a 0.05 $M_\odot$ step. We match the track's metallicity to that of the clusters: solar-metallicity tracks are used for the Pleiades, NGC 6811, NGC 6819 and M67; [Fe/H] = +0.1 tracks are used for Ruprecht 147; [Fe/H] = +0.2 tracks are used for Praesepe.

We launch each track using values of $P_{\rm init}$ obtained from a 1D smoothing spline fit to the median percentile in Upper Sco (Figure 1) at the track's stellar mass. We allow for core-envelope decoupling for all stars except fully convective ones, which are modeled as rigid rotators due to the lack of a distinct core. We interpolate $T_{\rm eff}$ and $P_{\rm rot}$ as a function of age and evaluate them at the ages of the clusters. We obtain a gyrochrone by further interpolating $P_{\rm rot}$ and $T_{\rm eff}$ across the full stellar mass range.

We quantify agreement between the model and observed $P_{\rm rot}$ by computing the $\chi^2 = \sum(P_{\rm obs} - P_{\rm mod})^2/\sigma_P^2$, where σ_P is the error on $P_{\rm obs}$ and is assumed to be 10% of $P_{\rm obs}$ (C. R. Epstein & M. H. Pinsonneault 2014). We normalize the χ^2 computed for each cluster by the number of data points used in the cluster's fit such that each cluster's χ^2 has an equal weight in the total $\chi^2_{\rm tot} = \chi^2_{\rm Pleiades} + \chi^2_{\rm Praesepe} + \chi^2_{\rm NGC6811} + \chi^2_{\rm NGC6819} + \chi^2_{\rm Rup147} + \chi^2_{\rm M67}$.

Thus, the fit includes 410 data points and three free parameters, f_k, $\omega_{\rm sat}$, and α. The best-fitting values of the parameters ($f_K = 10.8$, $\omega_{\rm sat} = 3.83 \times 10^{-5}$, and $\alpha = 9.53$; $\chi^2_{\rm tot} = 25$) are obtained by minimizing $\chi^2_{\rm tot}$ through the differential evolution (`DE`) function from the Python library `yabox` (P. R. Mier 2017). The calibrated gyrochrones evaluated at the clusters' ages are shown in Figure 2.

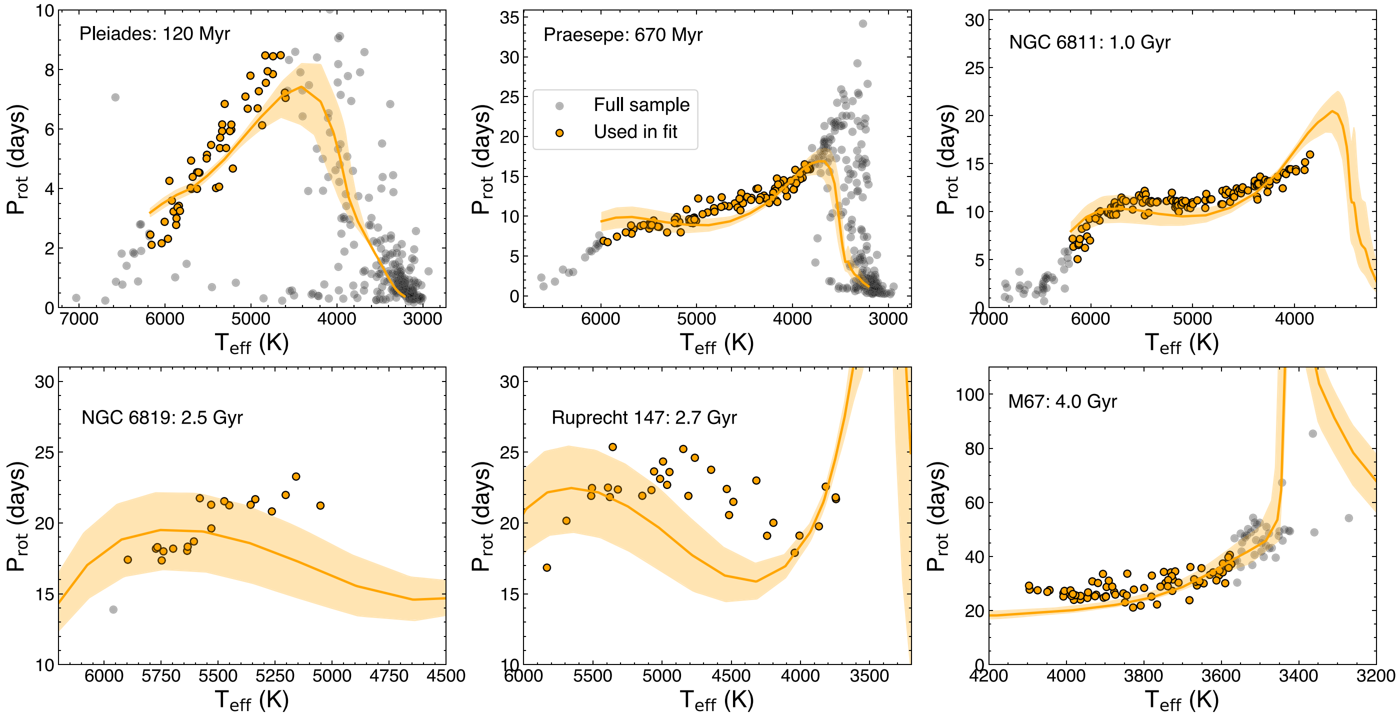

Figure 2. Gyrochrones launched from the median percentile of the Upper Sco distribution of initial rotation periods are shown as a solid orange line in each plot against observed cluster member rotational sequences. These gyrochrones are fit to the cluster's observed periods of stars that have converged onto the cluster's rotational sequence. Shaded regions around each gyrochrone account for the uncertainty in the cluster's age at which the models are being evaluated. Note that the values of $P_{\rm rot}$ and $T_{\rm eff}$ in these clusters do not span the same range.

2.2. White-dwarf Cosmochronology

White dwarfs are the final evolutionary stage of stars with initial masses of less than roughly 8–10 $M_\odot$. Because they no longer undergo nuclear fusion in their cores, their evolution consists of a cooling phase dominated by the leaking of residual thermal heat from the nondegenerate ions in the electron-degenerate core. The key idea behind using WDs as cosmochronometers is that their effective temperature and mass map uniquely onto a single cooling age. The effective temperature and surface gravity of the WD, which yield its mass, can be derived from either spectroscopy or photometry coupled with model atmospheres. Once the cooling age has been determined using the WD atmospheric parameters, the next step is to estimate its progenitor MS and post-MS lifetimes. This is done by using IFMRs (e.g., J. D. Cummings et al. 2018) to correlate the final WD mass to initial ZAMS masses, from which the progenitor lifetimes are estimated. The total age of the WD is given by the sum of the cooling age and progenitor MS and post-MS lifetimes.

For WDs with available spectral classification (99 out of a total of 185 WDs), we adopt the appropriate cooling sequences and atmospheric models. If no spectral information is available, we assume a DA (hydrogen-rich) spectral type. The assumption that a non-DA WD is a DA can introduce a systematic mass error of 10%−15% (N. Giammichele et al. 2012); however, due to the lack of spectral information for these WDs, this is the simplest assumption that we can adopt. Spectral types are listed in Table 1 in Appendix B.

Due to the lack of spectroscopic observations for all the WDs in the sample, we use spectral energy distribution (SED) fitting of the mean fluxes in different bands from all-sky surveys including Gaia, the Sloan Digital Sky Survey (SDSS), the Panoramic Survey Telescope and Rapid Response System (PanSTARRS), and the SkyMapper Southern Survey. We compute total ages of the WDs following the methods outlined in T. M. Heintz et al. (2022), which we summarize below for completeness.

2.2.1. Fitting Routine

For DA WDs and WDs with no determined spectral type, we convert model DA white-dwarf spectra, spanning effective temperatures of 3000–40,000 K and surface gravities of 6.25–9.5 dex, from D. Koester (2010) to synthetic fluxes by using the sensitivity of each bandpass and the appropriate AB magnitude zero-points. Following O. Vincent et al. (2024) and T. M. Heintz et al. (2024), we use pure He models from E. Cukanovaite et al. (2021) for all DBs, all DQs, and DCs and DZs above 11,000 K, and mixed model atmospheres with H/He ratios of 10^{-5} from E. Cukanovaite et al. (2021) for all DBAs and DCs and DZs between 5500 and 11,000 K. For DCs and DZs below 5500 K, the same DA models discussed above are used. The observed magnitudes are also converted to absolute fluxes at 10 pc using AB zero-points and the weighted mean parallax of the binary from Gaia. For SDSS u and z, the magnitudes are shifted 0.04 and 0.02 mag, respectively, to account for the shift relative to the AB mag system (K. Abazajian et al. 2004). The weighted mean parallax of the binary system is dominated by the brighter MS star and is on average 6 times more precise than the individual WD parallax, which in turn allows for a more precise age determination. The observed fluxes are dereddened using extinction values from N. P. Gentile Fusillo et al. (2021), which are obtained using the 3D extinction maps from R. Lallement et al. (2022). These observed dereddened fluxes are related to the model synthetic fluxes through the radius of the WD (P. Bergeron et al. 2019) through the following relation

$$F_X = \frac{R^2}{(3.08568 \times 10^{19}\ \mathrm{cm})^2} F_{X,\mathrm{mod}}(T_{\mathrm{eff}}, \log g) \quad (6)$$

where F_X is the observed flux at 10 pc in bandpass X, R is the radius of the WD in centimeters, and $F_{X,\mathrm{mod}}$ is the synthetic flux in bandpass X that is a function of effective temperature and surface gravity. The denominator is 10 pc in units of centimeters.

We use a Markov Chain Monte Carlo (MCMC) approach and make use of the Python package emcee (D. Foreman-Mackey et al. 2013) to get best-fit temperatures and radii, which are represented by the 50th percentiles of the MCMC posterior distributions. These are converted to surface gravities, masses, and cooling ages using the "thick" cooling models from A. Bédard et al. (2020) for the WDs with hydrogen atmospheres, which assume that the WD inherits a thick hydrogen layer from its progenitor and thus retains its DA spectral type throughout its life. For the mixed and pure He atmosphere fits, the "thin" cooling models from A. Bédard et al. (2020) are used. We use flat priors for the temperatures and surface gravities that cover the full range of the models. A lower limit on the magnitude uncertainties of 0.03 mag is set to account for systematics in the conversion of magnitudes to average fluxes. We also impose a lower limit on the uncertainty on the surface gravities of 0.03 dex and a lower uncertainty of 1.2% on the effective temperatures to account for any unknown systematics in the models (e.g., J. Liebert et al. 2005).

2.2.2. Photometric Cleaning

There is often a large luminosity contrast between the WD and the MS star in the binary; therefore, an added measure of cleaning of the photometry is needed to obtain reliable parameters. We first remove photometry that is flagged for several issues in SDSS, PanSTARRS, and SkyMapper. We remove photometry from SDSS with EDGE, PEAKCENTER, SATUR, and NOTCHECKED flags. We only use photometry from PanSTARRS with rank detections of 0 or 1. We also remove any photometry from SkyMapper that has any raised flags.

Going beyond our method in T. M. Heintz et al. (2022), we also systematically remove photometric SED points that are not consistent with the Gaia fluxes in an effort to remove WD photometry that is contaminated by the MS companion. To do this, after running the fitting routine described in Section 2.2.1, we then fit a line to the residuals of the resulting SED fit to search for any incorrect temperature estimates due to contaminated photometry. We take the percent difference between the linear fit and the residuals of the SED fit to find photometric bands that are inconsistent with the Gaia fluxes. Any photometric bands that are more than 3σ away from the largest percent difference between the Gaia residuals and the linear fit are removed, where σ is the uncertainty for the individual photometric band. We then repeat the process with these photometric bands removed and iterate until a consistent list of suspect photometric bands are determined. Then, a final SED fit is performed with these bands removed. This process mainly removes redder photometry that has been contaminated by the MS companion. SDSS u band is not subjected to this stage of photometric cleaning since it can be a strong indicator of whether the WD is a DA or non-DA due to the presence of the Balmer jump in DA WDs. The larger residual of SDSS u can be indicative of a non-DA and not because the photometry is suspect (e.g., P. Bergeron et al. 2019). We find that 30 WDs show anomalously discrepant SDSS u-band photometry that suggests there may be some non-DAs in the sample. However, since >65% of WDs in the Gaia magnitude-limited samples are DAs (S. J. Kleinman et al. 2013a), adopting a DA model is a reasonable assumption.

Moreover, T. M. Heintz et al. (2022) found that, when assuming DA spectral types for all the WDs in their sample, the ages are good to 25% and provided error inflation factors to account for inaccuracies in the WD ages, including the assumption of an incorrect spectral type.

2.2.3. Progenitor Lifetimes

To get the progenitor lifetimes of the WDs, we use an IFMR from T. M. Heintz et al. (2022), which uses a theoretically motivated shape to the IFMR from C. E. Fields et al. (2016), fit to WDs in solar-metallicity clusters (J. D. Cummings et al. 2015, 2016), in conjunction with the stellar evolutionary tracks from Modules for Experiments in Stellar Astrophysics (MESA; B. Paxton et al. 2011, 2013, 2015). The errors on these values are determined by using the 1σ uncertainties on the WD mass to determine an upper and lower MS mass. The difference between the central value and the upper and lower MS mass is quoted as upper and lower errors, respectively. The same process is carried out for the progenitor lifetimes, as well.

2.2.4. Precision of Total Ages

The total age of the WDs in the sample is primarily determined by their mass, and therefore uncertainties in the WD mass have a significant impact on the accuracy of the estimated total ages. T. M. Heintz et al. (2022) found that the total ages derived from WDs with $M < 0.63\,M_\odot$ become very noisy. Moreover, accurately determining the ages of low-mass WDs poses a challenge due to the lack of well-defined constraints at the lower end of the IFMR. WDs with masses below $0.575\,M_\odot$ may not provide reliable age estimates since they might not have formed through the evolution of a single star. While their cooling ages can offer a minimum estimate of their total age, it is essential to consider the possibility that their low mass is a result of contamination in the photometry, especially if they are formed through binary interactions.

Thus, we adopt the following: we ignore total ages obtained from WDs with $M < 0.575\,M_\odot$; for WDs with $M > 0.575\,M_\odot$, we adopt the total ages computed as the sum of the cooling age and progenitor lifetimes. To avoid contamination from the MS companion, we filter sources with a Gaia BP − RP corrected excess factor <0.1 (M. Riello et al. 2021). Because formal age uncertainties are often underestimated for higher-mass WDs, we inflate the age uncertainties by a factor computed following the comparison to wide WD+WD described in T. M. Heintz et al. (2022).

Our final sample predominantly comprises massive WDs (with masses greater than $0.67\,M_\odot$), in which the total ages are primarily influenced by cooling rather than the IFMR, as illustrated in Figure 3. This results in an average age uncertainty of 10% prior to inflation and 20% post inflation.

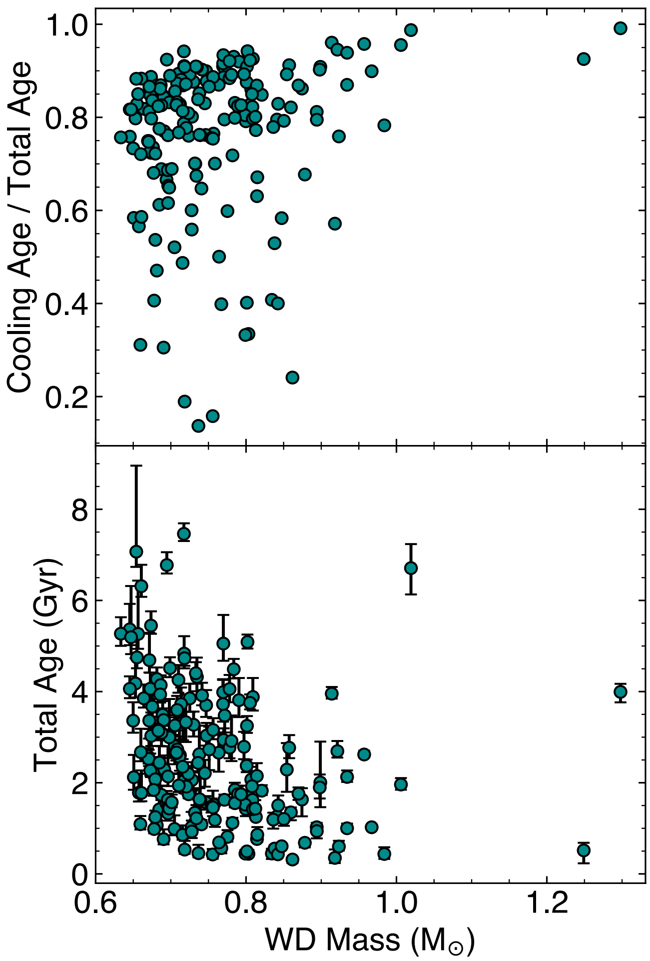

Figure 3. Top: contribution of the cooling age to the total age of the WD as a function of mass. Bottom: WD total age as a function of mass; the uncertainties on the WD ages have been inflated by empirically determined factors (T. M. Heintz et al. 2022) to compensate for systematics on the total ages.

3. Sample Selection

We construct the wide binary sample using the K. El-Badry et al. (2021) catalog, which contains 1.3 (1.1) million binaries with a >90% (>99%) probability of being bound. Stars are classified as MS or WD based on their location on the Gaia color–absolute magnitude diagram (CMD). The absolute magnitude is defined as $M_G = G + 5\log(\omega) - 10$, where G is the G-band mean magnitude and ω is the parallax in milliarcseconds; stars with $M_G > 3.25(G_{\rm BP} - G_{\rm RP}) + 9.625$ are classified as WDs; all other stars with measured $G_{\rm BP} - G_{\rm RP}$ are classified as MS stars (K. El-Badry & H.-W. Rix 2018). We only select systems containing a WD and an MS star and find 22,563 such systems.

We search for rotation periods of these MS stars in several rotation surveys, including the Asteroid Terrestrial-impact Last Alert System (ATLAS) variable stars database (A. N. Heinze et al. 2018), the All-Sky Automated Survey for SuperNovae (ASAS-SN) variable star database (B. J. Shappee et al. 2014; T. Jayasinghe et al. 2018), the CARMENES catalog (E. Díez Alonso et al. 2019), the Gaia third Data Release (DR3, Gaia Collaboration 2022), the HATNet Exoplanet survey (J. D. Hartman et al. 2010), the KELT database (R. J. Oelkers et al. 2018), the Kepler (A. McQuillan et al. 2014b; A. R. G. Santos et al. 2020, 2021) space mission, the K2 space mission (T. Reinhold & S. Hekker 2020), the MEarth Observatory (E. R. Newton et al. 2016, 2018), and the Zwicky Transient Facility (ZTF, X. Chen et al. 2020; Y. L. Lu et al. 2022). We find 5005 binaries that feature an MS star with a measured rotation period, with approximately 85% of the rotation periods sourced from the ZTF catalog. Y. L. Lu et al. (2022) found that nearly 50% of stars with ZTF periods <10 days are likely to be incorrect; therefore, we exclude all binaries with such ZTF fast rotators. This reduces the number of WD + MS systems with measured rotation periods to 2701.

We crossmatch these MS stars with various spectroscopic catalogs, including the Galactic Archaeology with HERMES (GALAH) survey (S. Buder et al. 2018), the Large Sky Area Multi-Object Fiber Spectroscopic Telescope (LAMOST; J. Zhong et al. 2020), the Apache Point Observatory Galactic Evolution Experiment (APOGEE) survey (Abdurro'uf et al. 2022), and Gaia DR3 (A. Recio-Blanco et al. 2023). We retrieve spectroscopic properties for 430 MS stars. We use spectroscopic data when available, but do not require spectroscopy to be included in the sample.

We obtain WD ages for these 2701 binaries. We require the final sample to meet the following criteria: $P_{\rm rot} > 10$ days to avoid contamination by tidally synchronized binaries (G. V. A. Simonian et al. 2019); WD mass $>0.575\,M_\odot$, since the total ages of the lowest-mass WDs are too uncertain (T. M. Heintz et al. 2022); Gaia BP − RP excess factor <0.1 (see Section 2.2.4 for more details); chance alignment factor calculated in K. El-Badry et al. (2021) `R_chance_align` <0.1 to remove binary pairs with high likelihood of being chance alignments; average of the uninflated low and upper uncertainties less than 20%. The final sample contains 185 wide binaries with precise WD ages, which we report in Table 1 in Appendix B. Among these, only 55 binaries have separations less than 1000 au. Furthermore, just 14 of these systems have separations less than 500 au, and only one has a projected separation under 200 au. At these distances, it is unlikely that wind Roche-lobe overflow has influenced the MS companion (B. Willems & U. Kolb 2004; A. Rebassa-Mansergas et al. 2013); therefore, the properties of the MS stars in our sample should resemble those of single MS stars since they have had no influence from their white-dwarf companions.

The distribution of rotation periods across the different catalogs used to create the sample is presented in Figure 4. We correct $G_{\rm BP} - G_{\rm RP}$ colors for extinction as in J. L. Curtis et al. (2020) and use them to compute the effective temperatures through the polynomial fit to the empirical color–temperature relation in J. L. Curtis et al. (2020). Their color–temperature relation was constructed using nearby benchmark stars, including a sample of low-mass stars with $3056\,{\rm K} < T_{\rm eff} < 4131\,{\rm K}$ and $-0.54\,{\rm dex} < [{\rm Fe/H}] < +0.53\,{\rm dex}$ from A. W. Mann et al. (2015). The basic properties and CMD of the sample are shown in Figures 5 and 6, respectively.

4. Results and Discussion

4.1. Model Assessment

In general, our gyrochrones reasonably match the rotation sequences observed in the clusters, with a few exceptions. For instance, for K dwarfs with effective temperatures between 4250 and 5000 K in Praesepe, our models predict rotation periods that are a few days shorter than those observed. Praesepe is a metal-rich cluster (V. D'Orazi et al. 2020). We

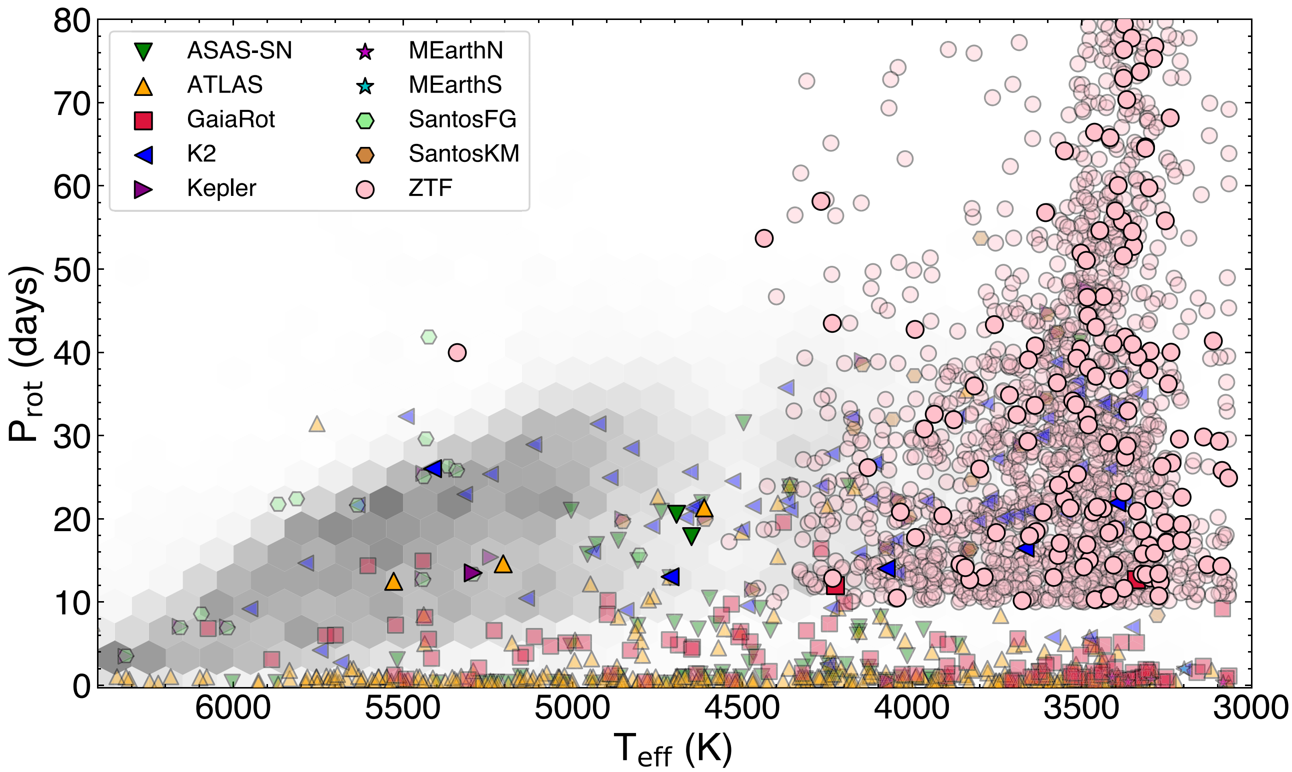

Figure 4. MS stars in the full wide WD+MS sample in T_{eff}–P_{rot} space. In all, 1985 rotation periods are retrieved from ZTF; 384 periods are from ATLAS; 102 periods are from Gaia DR3; K2 provides 82 periods; 78 periods are from ASAS-SN; 23 periods are retrieved from Kepler; 15 periods are from A. R. G. Santos et al. (2021); 20 periods are from A. R. G. Santos et al. (2020); 9 periods are from MEarth North, and 3 periods are from MEarth South. The most opaque markers represent the MS stars in the WD + MS binaries that made it into the final selection (185 systems) described in Section 3. The McQuillan Kepler field (A. McQuillan et al. 2014a) of 34,030 MS stars below 6500 K is shown in the background, together with the additional detection of 15,640 M- and K-type Kepler stars by A. R. G. Santos et al. (2019).

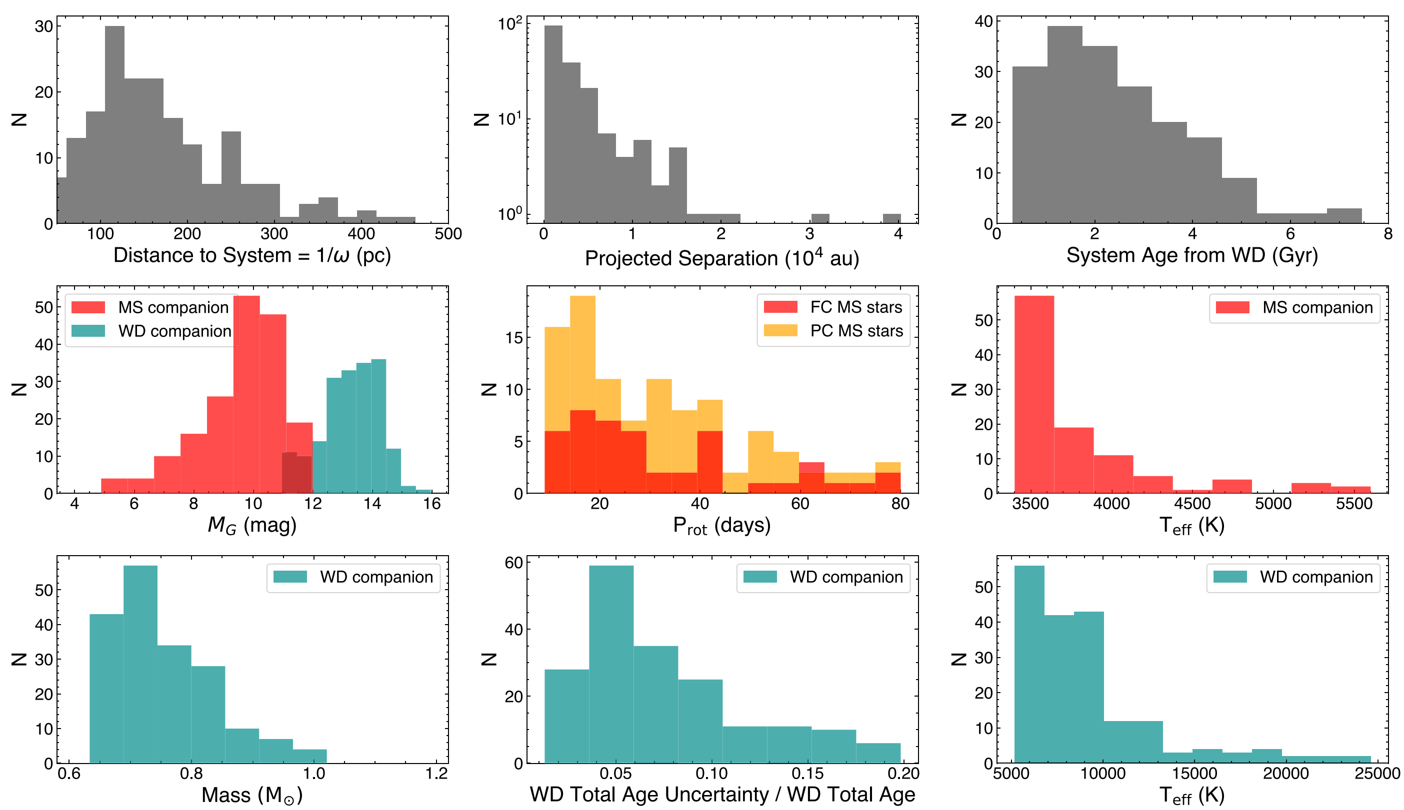

Figure 5. Properties of the 185 binaries with precise WD ages in the sample. We distinguish fully convective (FC) MS stars from partially convective (PC) MS stars based on their absolute Gaia magnitude, M_G, and Gaia BP − RP color measurements using Jao's gap (W.-C. Jao et al. 2018).

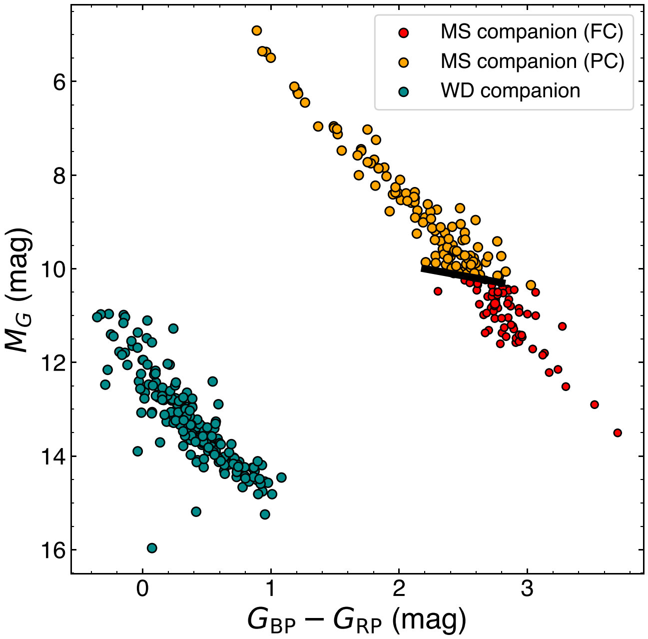

Figure 6. Gaia color–magnitude diagram showing the sample of 185 WD + MS binaries with the most precise WD total ages (average uncertainty <10%). The W.-C. Jao et al. (2018) gap is shown as a solid black line.

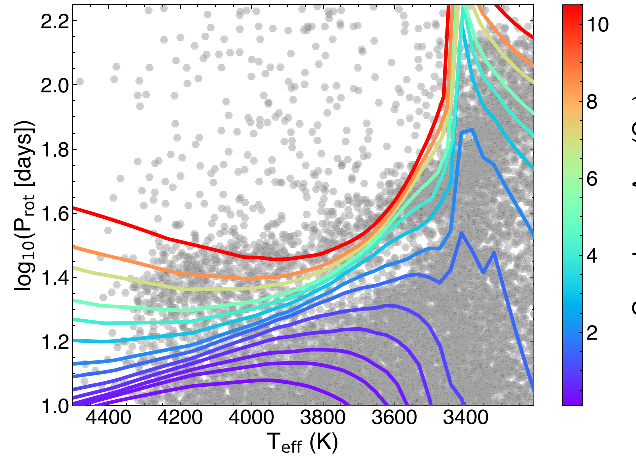

Figure 7. ZTF stars from Y. L. Lu et al. (2022) are plotted as gray circles. Our gyrochrones are shown as solid lines and color coded by their age. The gyrochrones are constructed using a non-spotted solar-metallicity grid and launched from the median P_{init} percentile in Upper Sco. For convenience, selected gyrochrones for a wide range of ages are provided in Appendix C.

note that there are no supersolar metallicity atmospheric tables available from F. Allard et al. (1997); therefore, we have approximated the metal-rich case with the solar atmosphere. However, we do not get very different best-fit parameters if we use solar-metallicity tracks for all clusters, including Praesepe. Furthermore, the rotational sequences of NGC 6819 and Ruprecht 147, which are roughly coeval, show discrepancies with our fit models.

Between the ages of Praesepe and Ruprecht 147, core-envelope coupling is important. The fit coupling timescale in this work has a strong mass dependence; therefore, lower-mass stars, such as K dwarfs poorly fit by our models, take an extended period before resuming their spindown. Here, we adopt a constant, rotation rate independent coupling timescale, although we expect this timescale to change with time. Additionally, our coupling model is not tuned for clusters older than 1 Gyr (F. Spada & A. C. Lanzafame 2020). J. L. Curtis et al. (2020) also found that the F. Spada & A. C. Lanzafame (2020) model underestimated the age for stars with $M < 0.7\,M_\odot$. We suspect that this coupling timescale prescription is contributing to the morphology mismatch between the rotational sequences of Praesepe, NGC 6819, and Ruprecht 147 and our models. The choice of coupling timescale prescription appears to be a more significant concern than differences in atmosphere or metallicity. Exploring more nuanced prescriptions that depend on evolutionary state and rotation rate are well motivated but beyond the scope of this work.

Another assessment of our models is presented in Figure 7, where we show a set of gyrochrones against the ZTF rotation-period catalog from Y. L. Lu et al. (2022). The ZTF distribution shows an overdensity of fully convective stars rotating slowly ($P_{rot} > 40$ days) past the closing of the intermediate period gap, a period dearth in the T_{eff}–P_{rot} space for low-mass stars that was first detected with Kepler by A. McQuillan et al. (2013). This increase in rotation period for such stars is also predicted by gyrochrones older than 2 Gyr. We note that while the apparent agreement with the ZTF is good, the earlier A. McQuillan et al. (2014a) sample contains stars with lower-amplitude modulation and slower rotation at these temperatures that are not fit by our gyrochrones. These stars are presumably older than 4 Gyr, and suggest that our core-envelope coupling prescription may be overly simplistic. Even if this is the case, it does not fundamentally alter the conclusions of this paper.

The best-fit parameters obtained from the clusters fit are in agreement with those from L. Cao et al. (2023; $f_k = 9.79 \pm 0.37$, $\omega_{sat} = (3.466 \pm 0.085) \times 10^{-5}$ rad s^{-1}, and $\alpha = 11.8 \pm 1.0$), who calibrated spotted models (G. Somers et al. 2020) to the Pleiades and Praesepe. We find a higher value of α compared to the value reported in F. Spada & A. C. Lanzafame (2020; $\alpha \approx 5.6$), although their models did not include stellar spots (which alter the mass–temperature relation and therefore apparent mass dependence of α) and assumed a fixed initial rotation period of 8 days for all stellar masses rather than a distribution of P_{init}. Moreover, their two-zone model has been calibrated for stellar masses down to $\approx 0.4\,M_\odot$.

4.2. A Spike in P_{rot} at the Fully Convective Boundary

Using the best-fit parameters, we construct gyrochrones to predict the rotation period of the stars in our sample at the age inferred from their WD companions. To make a direct comparison between model and observed rotation periods, we create a grid of $f_{spot} = 0\%$, solar-metallicity tracks for stellar masses between 0.18 and 1.15 $M_\odot$. The grid has a spacing of 0.01 $M_\odot$ for masses between 0.18 $M_\odot$ and 0.60 $M_\odot$ and 0.05 $M_\odot$ for masses between 0.60 $M_\odot$ and 1.15 $M_\odot$. For each stellar mass, we initiate a track with P_{init} values ranging from the 5th to the 95th percentiles, in steps of 1 percentile, of the Upper Sco period distribution (Figure 1). For each star in our data sample, the model rotation period $\overline{P_w}$ is computed as the likelihood-weighted average of the rotation periods in the grid

$$\overline{P_w} = \frac{\sum_{i=1}^{n} \Delta t_i \Delta m_i \mathcal{L}_i P_i}{\sum_{i=1}^{n} \Delta t_i \Delta m_i \mathcal{L}_i}, \tag{7}$$

where Δt_i and Δm_i are the time and mass increments between each point on our nonuniformly sampled model grid, respectively. P_i is the ith model rotation period in the grid; $\mathcal{L}_i$ is its corresponding likelihood, given by

$$\mathcal{L}_i = \exp\left\{-0.5\left[\left(\frac{T_{\rm eff,obs} - T_{\rm eff,i}}{\sigma_{T_{\rm eff,obs}}}\right)^2 + \left(\frac{A_{\rm obs} - A_{\rm i}}{\sigma_{A_{\rm obs}}}\right)^2\right]\right\}. \quad (8)$$

The likelihood function is computed for every grid point using its associated effective temperature $T_{\rm eff}$, i, and age $A_{\rm i}$. It also accounts for the uncertainty $\sigma_{A_{\rm obs}}$ on the WD age $A_{\rm obs}$, taken as the average of the inflated (as per T. M. Heintz et al. 2022) lower and upper uncertainties, and the uncertainty $\sigma_{T_{\rm eff,obs}}$ on the effective temperature $T_{\rm eff,obs}$ of the MS star. Uncertainty $\sigma_{T_{\rm eff,obs}}$ is computed as the root sum of the squares of the typical temperature precision (± 50 K) and the uncertainty obtained from propagation of the Gaia extinction-corrected $G_{\rm BP} - G_{\rm RP}$ uncertainties involved in the color–$T_{\rm eff}$ relation (J. L. Curtis et al. 2020).

Due to the lack of uncertainties in the observed rotation periods, we compute the likelihood-weighted standard deviation σ_w of the model periods to quantify the constraining power of our models on the rotation periods. Standard deviation σ_w is defined as

$$\sigma_w = \sqrt{\frac{\sum_{i=1}^{n} \Delta t_i \Delta m_i \mathcal{L}_i (P_i - \bar{P}_w)^2}{\sum_{i=1}^{n} \Delta t_i \Delta m_i \mathcal{L}_i}}. \quad (9)$$

The lower the ratio $|\Delta P_{\rm rot}/\sigma_w|$, the smaller the discrepancy between the observed and the predicted rotation periods is. The results are presented in Figure 8. A total of 65% of the rotation periods predicted by non-spotted, solar-metallicity models are within $3\sigma_w$ of the observed rotation periods and fall in the region bounded by the gyrochrones computed at the lower and upper WD age bounds in each bin.

At the FCB, our sample shows a rapid increase in the rotation period of MS stars with WD ages up to 7.5 Gyr. The same trend is confirmed by the gyrochrones ([Fe/H] = +0.0, $f_{\rm spot} = 0\%$), which span periods between 30 and 100 days across a narrow temperature range ($\sim$50 K) for ages up to 2.0 Gyr. Similarly, between 2.0 and 4.0 Gyr, the models show a sharp rise in rotation period from 50 to 200 days and up to 270 days between 4.0 and 7.5 Gyr. Thus, both the models and data suggest that, at the FCB, stars with relatively long rotation periods are not necessarily old, in contrast to the standard picture of stellar spindown. In addition, at this boundary, a measured rotation period cannot be uniquely associated (within reasonable observed errors in $T_{\rm eff}$ of $\simeq$50 K) to a single gyrochrone—rather, gyrochrones spanning several billions of years all provide reasonable matches to the observed ($P_{\rm rot}$, $T_{\rm eff}$) combination. This significantly inflates the age uncertainties on rotation-based ages in this $T_{\rm eff}$ range as the rotation period of a star along this vertical incline is predicted, within 1σ, by gyrochrones between 2 and 8 Gyr.

Beyond the FCB, our models return to a reasonable behavior without distinct features. This suggests the feasibility of applying gyrochronology to the coolest fully convective stars, at least from a model standpoint.

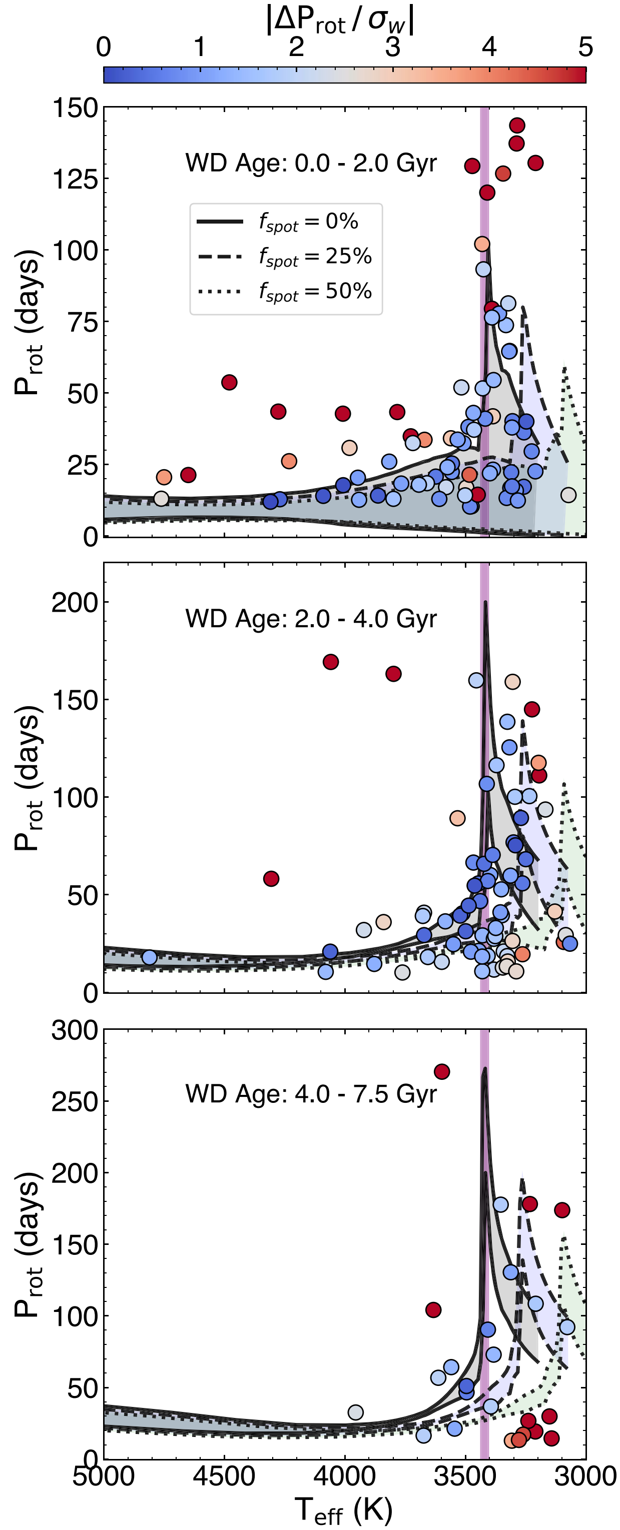

Figure 8. MS stars binned by their companion WDs ages. The gray-shaded regions show the range of rotation periods spanned by $f_{\rm spot} = 0$, solar-metallicity gyrochrones launched from the median percentile of Upper Sco at the WD age bounds, which are plotted as black solid lines. Gyrochrones with $f_{\rm spot} = 25\%$ and $f_{\rm spot} = 50\%$ launched with the same $P_{\rm init}$ at the same ages are plotted as black dashed and dotted lines, respectively, and the corresponding region of allowed rotation periods is shown in light pink and green. The vertical purple band represents the fully convective boundary. Stars are color coded by $|\Delta P_{\rm rot}/\sigma_w|$ (see Section 4.2). Blue points show good agreement, while the redder points show worse agreement between the observed and the predicted rotation periods.

4.3. Model Description of the Spike

Stellar interior theory predicts that as the stellar mass decreases, the convection zone (CZ) deepens in the interior of the star until the star becomes fully convective at $\sim 0.35\, M_\odot$. The convective overturn timescale refers to the characteristic timescale of convective motions. In this work, we compute the characteristic convective overturn timescale as the local $\tau_{cz} = H_P / v$, where H_P is the pressure scale height at the base of the convective zone and v is the convective velocity (from a mixing-length theory of convection) one pressure scale height above the convective zone boundary. As we approach the FCB, the convective envelope gets deeper, occupying a larger part of the total stellar mass, the pressure scale height increases, and the convective velocity decreases, as predicted by the mixing-length theory (E. Böhm-Vitense 1958). This leads to an increase in τ_{cz}.

However, it has been shown that the behavior of models near the transition to the fully convective regime is not smooth. The J. L. van Saders & M. H. Pinsonneault (2012a) instability predicts that low-mass stars at the boundary undergo nonequilibrium ^{3}He burning, which gives rise to a small convective core separated from the convective envelope by a thin radiative zone. As the amount of central ^{3}He increases, the convective regions grow in mass and the convective envelope deepens, until they merge, leading to a fully convective episode. This process repeats until the total ^{3}He concentration is high enough that the star remains fully convective.

In the models used in this work, the J. L. van Saders & M. H. Pinsonneault (2012a) instability occurs for masses between $0.30\, M_\odot$ and $0.37\, M_\odot$, depending on the metallicity and spot covering fraction. For instance, in a solar-metallicity, $f_{\rm spot} = 25\%$ model grid, the J. L. van Saders & M. H. Pinsonneault (2012a) instability affects models in the $0.31-0.34\, M_\odot$ range and the FCB is at $0.31\, M_\odot$ (i.e., stars with $M < 0.31\, M_\odot$ never have a radiative core). This is shown in Figure 9. In the top panel, we see that as we move from a $0.4\, M_\odot$ partially convective star to $0.31\, M_\odot$, the contribution of the mass of the convective zone to the total stellar mass increases, until the star is fully convective and $M_{cz}/M_{\rm tot} = 1$. Similarly, the middle panel shows that the base of the convective zone is eating downward in mass and deepening in the interior as we approach the FCB, which makes $\tau_{\rm cz}$ longer. Furthermore, due to fully convective episodes initiated by nonequilibrium ^{3}He burning, the convective zone base of stars in the range $0.34 - 0.31\, M_\odot$ suddenly moves from a fractional depth $R_{cz}/R_{\rm tot} = 0.4-0.3$ to the center of the star $R_{cz} = 0$, which results in discontinuous jumps in τ_{cz}, as seen in the bottom panel. The convective overturn timescale maxima are in phase with drops in $R_{cz}/R_{\rm tot}$ and peaks in $M_{cz}/M_{\rm tot}$ and correspond to fully convective episodes.

We suggest that it is the rise in $\tau_{\rm cz}$ due to differences in the structure of partially and fully convective stars that causes the vertical feature in $P_{\rm rot}$ for low-mass stars older than 1 Gyr, and that its sharpness is caused by the fact that the CZ boundary does not smoothly move toward the core (as a function of mass) until the star is fully convective, but rather jumps from a partially convective configuration in stars undergoing the J. L. van Saders & M. H. Pinsonneault (2012a) instability.

To show how $\tau_{\rm cz}$ affects stellar spindown at the FCB, we consider the relative contribution of all terms involved in the braking law. We evaluate the weight of the factors affecting dJ/dt, computed as shown in Equations (3) and (4), as a function of stellar mass at the median age of the data sample ($\sim$2 Gyr). Since the majority of the stars in the sample are M dwarfs that slowly evolve on the main sequence and the structure is very stable after the fully convective episodes, the contribution of the structural terms in the braking law do not significantly depend on the age at which they are evaluated. The results are shown in Figure 10: while the stellar mass, radius, luminosity, and pressure factors vary smoothly for stars with masses between $1.15\, M_\odot$ and $0.2\, M_\odot$, the convective overturn timescale factor changes abruptly at the FCB, between $0.33\, M_\odot$ and $0.31\, M_\odot$. In this narrow mass range, $\tau_{\rm cz}$ rapidly increases as we approach $0.33\, M_\odot$, reaches a peak at $0.31\, M_\odot$, and then drops modestly. No other stellar property exhibits such a distinct feature at this boundary.

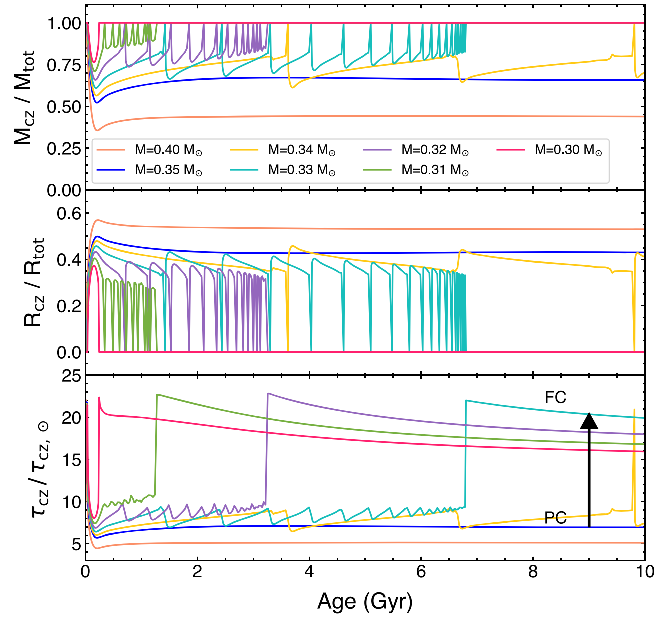

Figure 9. The sizes of the convective zone relative to the total size of the star in mass and radius coordinates as a function of time are plotted in the top and middle panels, respectively. The bottom panel shows the convective overturn timescale normalized by the solar value as a function of time. The black arrow shows the jump between partially convective (PC) and fully convective (FC) stars. In all panels, the saw-toothed curves represent stars undergoing fully convective episodes driven by nonequilibrium ^{3}He burning (J. L. van Saders & M. H. Pinsonneault 2012a). All tracks have solar metallicity and a 25% spot covering fraction.

The peak in the $\tau_{\rm cz}$ curve in the bottom panel of Figure 10 is reached by the model with the largest mass—and thus largest H_P—that becomes fully convective, which is the $0.31\, M_\odot$ model in the solar-metallicity, $f_{\rm spot} = 25\%$ model grid. Below this point, stars are fully convective since they never have a radiative core. However, they are also smaller in radius and mass of the CZ, therefore $\tau_{\rm cz}$ drops. Figures 19 and 20 showing the rotational evolution of stars affected by the J. L. van Saders & M. H. Pinsonneault (2012a) instability at the boundary in conjunction with changes in their $\tau_{\rm cz}$ are included in Appendix A.

4.3.1. Calibrations for $\tau_{\rm cz}$ across the Fully Convective Boundary

Literature sources do not agree on a single method for computing the convective overturn timescale from a stellar model, but we argue here that the sharp increase in the convective overturn timescale that drives rapid braking is a

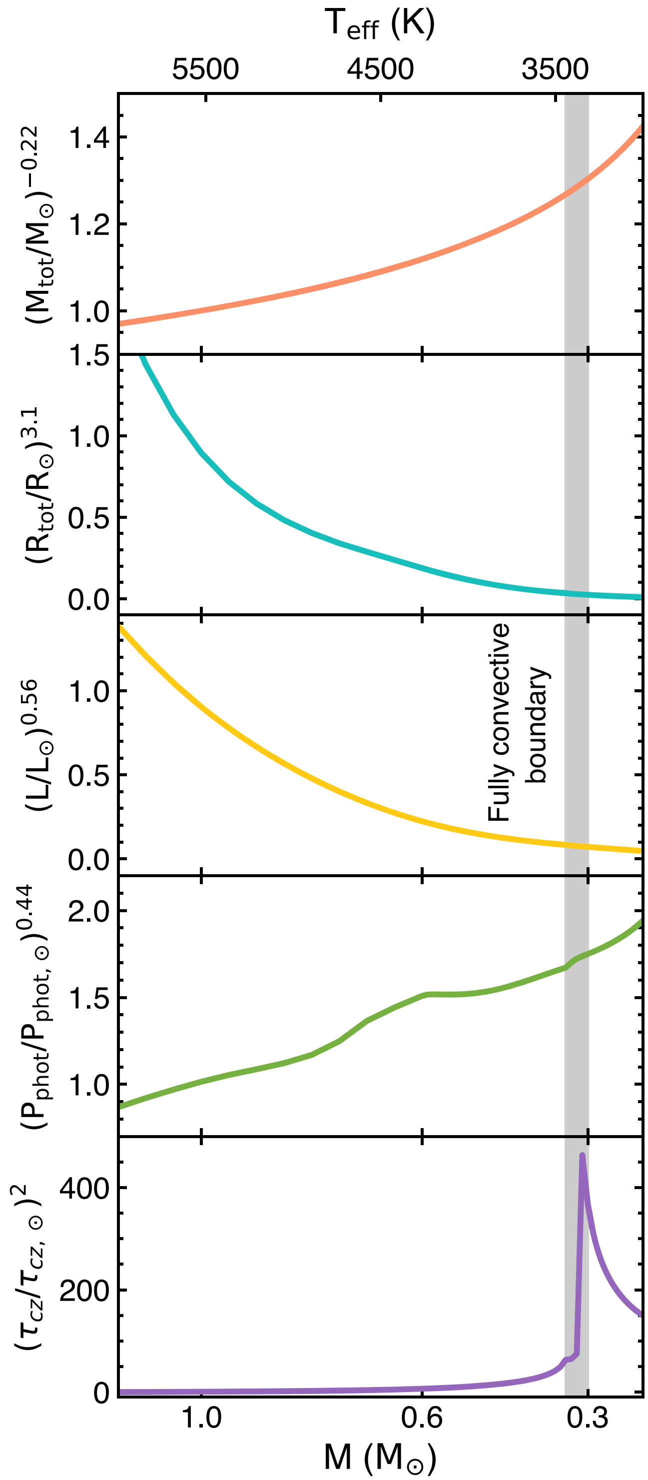

Figure 10. Contributions of the stellar mass M, radius R, luminosity L, photospheric pressure P_{phot}, and convective overturn timescale τ_{cz} factors to the total dJ/dt using solar-metallicity models with 25% spot covering fraction. The fully convective boundary is at $M = 0.31\ M_\odot$.

ubiquitous feature across common prescriptions for inferring the timescale.

When using models to compute convective overturn timescales, there are two primary approaches: the "local" prescription (used here) and a "global" prescription, where one instead computes some suitable average τ_{cz} over the entire convection zone. Both approaches yield fundamentally the same behavior modulo a scale factor, since the deep portions of the CZ probed by the local approach are also the most heavily weighted in the global average (Y.-C. Kim & P. Demarque 1996). We show in Figure 11 that our fiducial model, which uses a local approach, displays fundamentally the same behavior as that in S. A. Barnes & Y.-C. Kim (2010), which utilizes a global approach. Once normalized by their respective solar convective overturn timescales, both methods show the same behavior as a function of mass and a rapid increase in τ_{cz} near the FCB as the τ_{cz} computation begins to probe the structure of the near core.

While the location in mass (or temperature) of the sharp rise in τ_{cz} depends on properties like the metallicity and spot covering fraction, both produce only modest shifts in the precise location of the rise in τ_{cz}, also shown in Figure 11. In the case of metallicity, stars are more convective at higher metallicity but fixed mass, shifting the rise in τ_{cz} and onset of full convection to slightly higher masses in metal-rich stars, although this vertical feature does not significantly move in temperature, as shown in Figure 12. Adding spots to the surface of the model—which may be an important component in modeling young, low-mass stars (L. Cao et al. 2023)—decreases the observed effective temperature, with only modest impacts on the structure of the deep interior (see G. Somers & M. H. Pinsonneault 2015), which shifts the onset of deep convection and large τ_{cz} values to lower effective temperatures but not significantly lower stellar masses. We find that the maximum stellar mass undergoing fully convective episodes decreases with increasing spot covering fraction: $0.35\ M_\odot$ for 0% spot covering fraction; $0.34\ M_\odot$ for 25% spot covering fraction; $0.32\ M_\odot$ for 50% spot covering fraction. Furthermore, a higher spot covering fraction leads to a lower peak rotation period, which is a direct consequence of the onset of the ^{3}He instability shifting to lower masses and therefore lower convective overturn timescales, as shown in Figure 13. While the precise location of the steep rise in τ_{cz} depends on the model physics, the existence of a steep rise does not.

Finally, attempts to develop purely empirical calibrations of τ_{cz} also predict an increase in overturn timescale across the FCB. N. J. Wright et al. (2018) made the assumption that fully convective M dwarfs obeyed the same Ro–activity relation as partially convective stars, and then found the values of τ_{cz} as a function of color (mass) that minimized scatter in the Ro−X-ray luminosity relation. Although the resulting relation does not trace the model predictions exactly (Figure 11), it does indicate a reasonably steeply rising τ_{cz} across the FCB.

4.4. A Few Complications

We find that 25% of the MS stars shown in Figure 8 have $|\Delta P_{rot}/\sigma_w| > 3$, i.e., their rotation rate as predicted by our spindown model is at odds with the apparent system age given by the WD. This percentage goes down to 12% if we exclude MS stars with an effective temperature within 200 K of the FCB. We argue that these discrepancies may have multiple potential sources.

4.4.1. Stellar Spots

The model rotation periods of M dwarfs in our sample shown in Figure 8 were obtained using a model grid with solar metallicity and $f_{spot} = 0\%$. However, by adopting a model grid with a nonzero spot covering fraction, we can extend the region probed by our models to cooler temperatures, as shown in

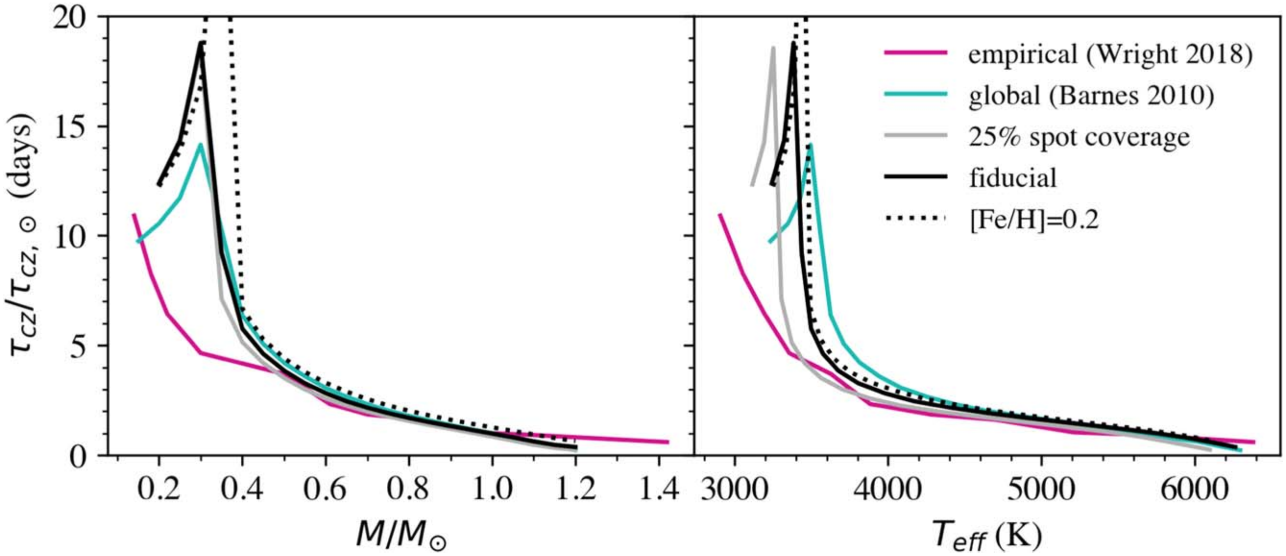

Figure 11. Comparisons of τ_{cz} values as a function of mass (left panel) and effective temperature (right panel). We show our fiducial, solar-metallicity unspotted stellar models as a solid black curve. Models with identical physics but a 25% spot covering fraction are shown in gray. The N. J. Wright et al. (2018) empirical calibration is shown in purple, and the S. A. Barnes & Y.-C. Kim (2010) "global" model-based τ_{cz} are shown in turquoise. Metal-rich ([Fe/H] = +0.2) models are shown as the dotted curve.

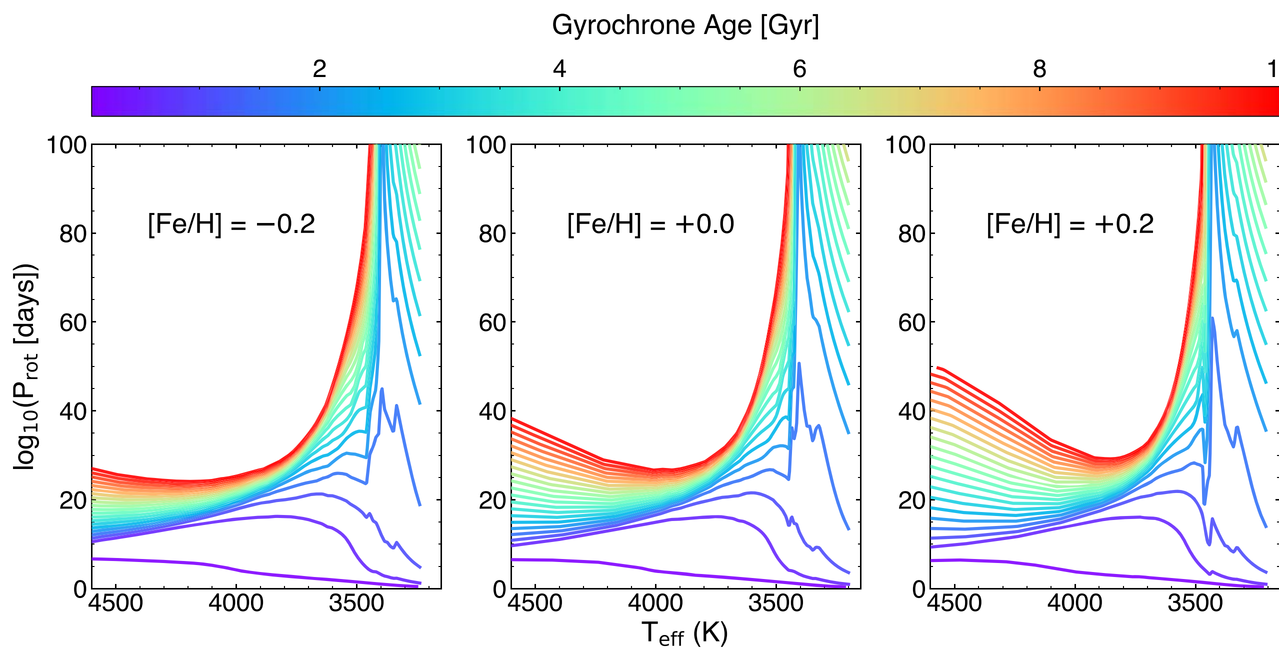

Figure 12. Gyrochrones constructed using a metal-poor (left), a solar-metallicity (center), and a metal-rich (right) non-spotted model grid. We show gyrochrones for ages between 0.1 and 10 Gyr, with a step of 0.5 Gyr. While the location of the steep rise in P_{rot} is shifted to slightly higher masses in metal-rich stars, the feature does not vary significantly in temperature and occurs at ≈3500 K across all model grids.

Figure 13. For instance, Figure 8 shows that some of the MS stars cooler than 3200 K that fall outside of the gray region bounded by the $f_{spot} = 0\%$ gyrochrones are found within the region bounded by the $f_{spot} = 25\%$ and $f_{spot} = 50\%$ gyrochrones. Therefore, knowing the f_{spot} of these stars would be helpful to choose the most appropriate tracks to model their spindown and improve the comparison between the predicted and observed rotation periods.

4.4.2. Metallicity

Metallicity may also be responsible for some of the discrepancies observed in our data. In the absence of spectroscopic data, we have assumed a solar metallicity for our sample. Modern braking laws, including the J. L. van Saders & M. H. Pinsonneault (2013) prescription used in this work, suggest that metallicity can have a strong impact on the rotational evolution of low-mass stars (L. Amard & S. P. Matt 2020; Z. R. Claytor et al. 2020). The convective overturn timescale is a direct consequence of the stellar structure and therefore is affected by the chemical composition of the star. Stars with a high abundance of elements heavier than He have a higher opacity, which steepens radiative temperature gradients, leading to deeper convective envelopes (L. Amard et al. 2019; J. L. van Saders & M. H. Pinsonneault 2012a), higher pressure scale height, and, therefore, a longer

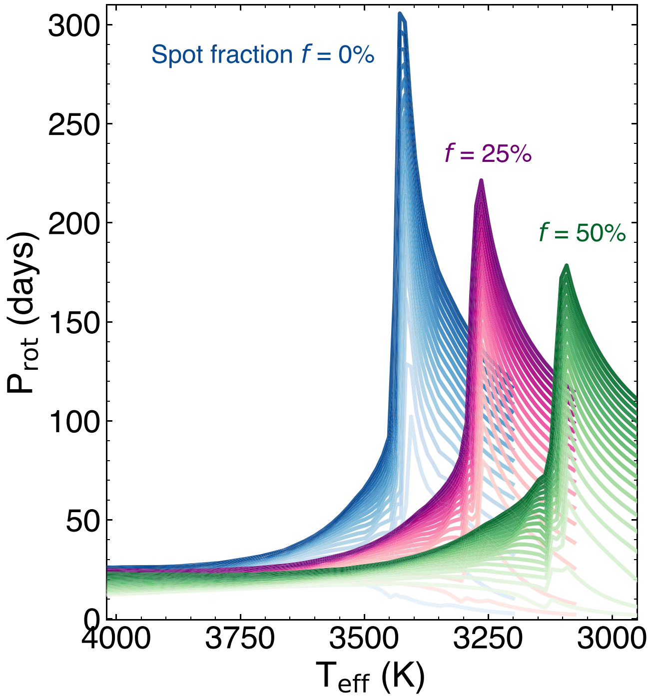

Figure 13. Solar-metallicity gyrochrones up to 10 Gyr constructed using three model grids with different spot covering fractions f_{spot}. The sharp rise in rotation period occurs for the same 0.30–0.34 $M_\odot$ mass range across the three model grids; however, the location of this feature varies across a ~350 K temperature window between the three model grids with different spot covering fractions.

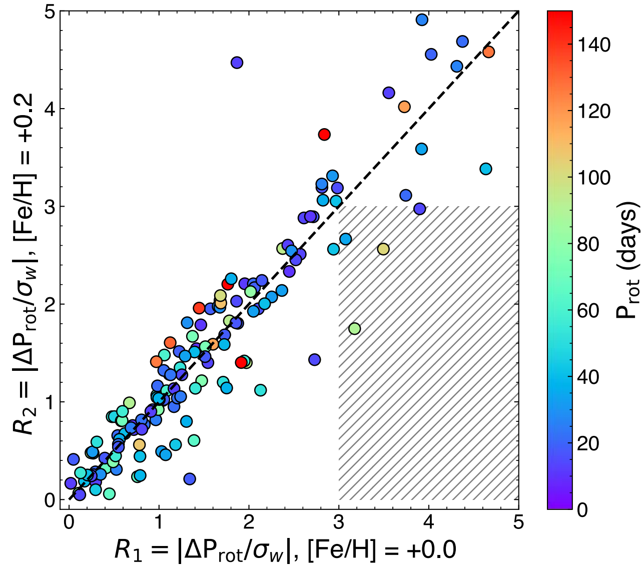

Figure 14. Comparison between $|\Delta P_{rot}/\sigma_w|$ computed for the MS stars in our sample using [Fe/H] = +0.0 and [Fe/H] = +0.2 model grids. Stars are color coded by their observed rotation period. A 1:1 line is plotted as a black dashed line. The hatched region in the bottom-right corner highlights stars for which $|\Delta P_{rot}/\sigma_w|$ decreases to $3\sigma_w$ or lower if a higher-metallicity model grid is adopted instead of a solar-metallicity one. Only a handful stars show improved values of $|\Delta P_{rot}/\sigma_w|$ when using an [Fe/H] = +0.2 model grid.

τ_{cz} and more efficient braking. We find that 57% of the stars with $|\Delta P_{rot}/\sigma_w| > 3$ have a positive ΔP_{rot} value, i.e., the MS stars' observed rotation periods are longer than the model periods. This percentage does not significantly change when not accounting for stars within 200 K from the FCB (44%).

Since higher metallicity leads to stronger braking, by adopting a metal-rich model grid we expect to recover longer model rotation periods that may provide a better match to the measured rotation periods. Figure 14 shows the difference between computing $|\Delta P_{rot}/\sigma_w|$ using a solar-metallicity model grid, like the one used in Figure 8, versus a higher-metallicity model grid. By adopting an [Fe/H] = +0.2 grid, we obtain an improvement in the predictions of rotation periods for only a handful of stars with $|\Delta P_{rot}/\sigma_w| > 3$ when computed with a solar-metallicity grid, as shown in Figure 14. Nevertheless, marginalizing over metallicity when constructing a model grid may improve the predictions of the rotation periods for systems with known metallicities.

Of the full sample, only 28 MS stars have measured metallicities. We find no evident trend with metallicity in those stars where measurements are available.

4.4.3. WD Age Resets in Triple Systems

We have neglected the possibility of triple systems where the inner WD binary merges and resets the apparent system age. Modeling the evolution of single star and binary populations has shown that the age of a merger remnant can be underestimated by a factor of 3 to 5 if single star evolution is assumed for a WD (K. D. Temmink et al. 2020). The same study found that WDs from binary mergers make up about 10%–30% of all observable single WDs and 30%–50% of massive (>0.9 $M_\odot$) WDs. Similarly, T. M. Heintz et al. (2022) estimated that 21%−36% of WD+WD pairs likely started as a triple system. These values are consistent with the fraction of binaries in our sample (≈30%) for which the models are unable to predict the rotation periods of the MS companions.

To test whether the discrepant systems in our sample may be reasonably accounted for by binary mergers, we create a synthetic population of 5000 stars with masses between 0.18 and 1.15 $M_\odot$ using the Chabrier functional form of the initial mass function (G. Chabrier 2003). For each star, we set the age to a random number between 0 and its MS lifetime (i.e., $t_{MS} = t_\odot (M/M_\odot)^{-2.5}$, $t_\odot \approx 10$ Gyr, which is consistent with the models' turnoff points). We find the point in our model grid that is closest to each age–mass combination and select the corresponding rotation period and effective temperature as the P_{rot} and T_{eff} of the stars in this synthetic population. Then, we randomly select 35% of the stars and reset their ages to a number between 0 and the original age drawn from a uniform distribution. This percentage is determined using the observed and estimated fractions of WD mergers reported by K. D. Temmink et al. (2020) and T. M. Heintz et al. (2022). We note that, for the purpose of this test, the age distributions of the synthetic population and our sample do not need to match since we are interested in testing whether we can reproduce the distribution of $\Delta P_{rot}/\sigma_w$ rather than that of the WD ages. The reset ages are used to compute $\Delta P_{rot}/\sigma_w$, as described in Equations (7) and (8).

We find that 16% of the MS stars in our data sample have a positive $\Delta P_{rot}/\sigma_w > 3$, i.e the age that we would infer from the rotation period of the MS star is older than what we estimate from their WD companions. The synthetic population reveals that 5% of the stars have a positive $\Delta P_{rot}/\sigma_w > 3$. The 2D histogram in the background of Figure 15 shows the distribution of $\Delta P_{rot}/\sigma_w$ as a function of the WD age after reset in the synthetic population and highlights a tail of

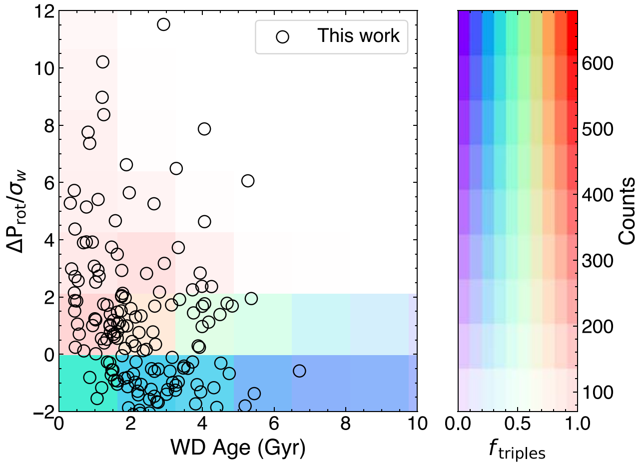

Figure 15. In the background, a 2D histogram shows the distribution of $\Delta P_{\rm rot}/\sigma_w$ relative to the ages of WDs in a sample drawn from a synthetic population. Each bin is color coded based on the fraction of triples (i.e., the number of WDs in the bin that have had their age reset), while the transparency reflects the total count of WDs in the bin. Warmer colors signify a higher proportion of WDs merger products, and greater opacity indicates a larger overall WD count in the bin. The black circles represent the distribution of the observed sample. At young WDs ages, the observed sample exhibits an increased occurrence of systems with $\Delta P_{\rm rot}/\sigma_w > 2$ in a region prone to triple contamination, as indicated by the synthetic population.

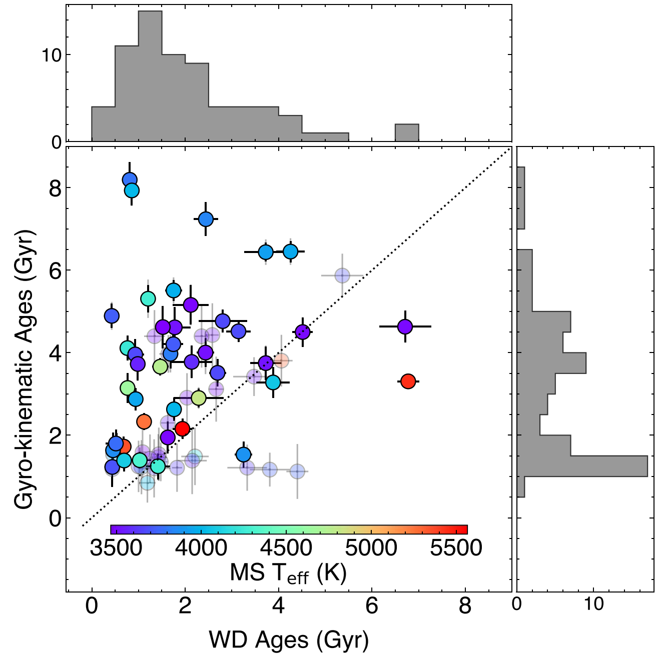

Figure 16. Comparison between the WD ages from this work and the median gyro-kinematic ages (Lu et al. 2021) for bins of Kepler stars around the MS stars in the sample. Data points are color coded by the effective temperature of the MS stars, with more transparent points indicating bins with at least 10 Kepler stars and more opaque points indicating bins with 30 or more Kepler stars. Uncertainties represent the upper and lower bounds on the WD ages, inflated as prescribed by Heintz et al. (2022). Histograms show the distributions of WD and gyro-kinematic ages.

discrepant $\Delta P_{\rm rot}/\sigma_w$ values at $t < 5$ Gyr in a region with a high fraction of triples per bin. Such a distribution is well matched by the distribution of $\Delta P_{\rm rot}/\sigma_w$ of our sample, as shown by the higher concentration of stars with $\Delta P_{\rm rot}/\sigma_w > 3$ at $t < 5$ Gyr and the decrease of the number of stars with $\Delta P_{\rm rot}/\sigma_w > 3$ with age.

While we cannot identify with certainty which WDs in our sample may be the products of binary mergers, our findings suggest that a fraction of the systems showing $\Delta P_{\rm rot}/\sigma_w > 3$ may have been triple systems that experienced merger events. Consequently, the ages we estimate for the WDs in such systems may underestimate the true system age, leading our models to predict shorter rotation periods for the companion MS stars than what is observed. We suspect, in particular, that the top panel of Figure 8 is subject to this bias, and that some significant portion of the long-period outliers may be these former triple systems.

4.5. Comparison to Other Data Sets

4.5.1. Gyro-kinematic Ages of Kepler Stars

We compare the WD ages with the empirical gyro-kinematic ages from Y. L. Lu et al. (2021). Gyro-kinematic ages leverage on the idea that the velocity dispersion of a stellar population at a given age increases with time due to gravitational interactions between the stars and gas clouds (L. Spitzer & M. Schwarzschild 1951). By making this assumption, Y. L. Lu et al. (2021) used the rotation periods of around 30,000 Kepler stars to determine their coeval nature (i.e., they assigned the same age to stars showing similar rotation periods and temperatures) and applied age–velocity-dispersion relations to estimate average stellar ages for groups of coeval stars.

We restricted our analysis to gyro-kinematic ages of stars with 3350 K $< T_{\rm eff} <$ 5000 K, where the gyro-kinematic ages should not be impacted by weakened braking (J. L. van Saders et al. 2019). To compare this sample to our WD + MS sample, for each MS star in our sample, we created a bin centered at its $P_{\rm rot}$ and $T_{\rm eff}$ and selected gyro-kinematic stars with a $P_{\rm rot}$ and a $T_{\rm eff}$ within 5 days and 100 K from the $P_{\rm rot}$ and $T_{\rm eff}$ of the MS star, respectively. If the bin did not contain a minimum number (10) of data points, we increased the size of the bin in the $P_{\rm rot}$ and $T_{\rm eff}$ directions by 10%; we repeated this process up to three times and until the bin contained a sufficient number of data points to obtain a median age representative of the gyro-kinematic age of the bin. We computed the gyro-kinematic age associated to the MS star in our sample as the median of the gyro-kinematic ages of the stars within the bin.

Figure 16 shows that there is a general disagreement between WD and gyro-kinematic ages. In particular, we identify two bands in the plot: a lower band, where the age predicted by the WD companion varies between 0.1 and 4 Gyr while the gyro-kinematic age is roughly constant at 1.5 Gyr, and an upper band, where the age inferred from the WD companions is younger than the gyro-kinematic age. Our hypothesis is that the elongation in the lower band may be due to core-envelope decoupling, which would cause these stars to have a similar rotation period but different ages. WDs more accurately track the true system age, while the gyro-kinematic age is confused by groups of stars with different ages having similar rotation periods. The discrepancies in the stars populating the upper band are likely caused by a combination of two factors: (1) some fraction of the WDs in our sample are WD merger products, and therefore the age inferred from the WD age is an underestimate of the true age of the system; (2) at the FCB, the gyrochrones are compressed, and therefore stars at the same rotation period along this boundary are not necessarily coeval.

We find that 30% of the stars located in this upper band show a $|\Delta P_{\rm rot}/\sigma_w| > 3$ and a positive $\Delta P_{\rm rot}$, which supports the WD merger hypothesis for these systems, as discussed in

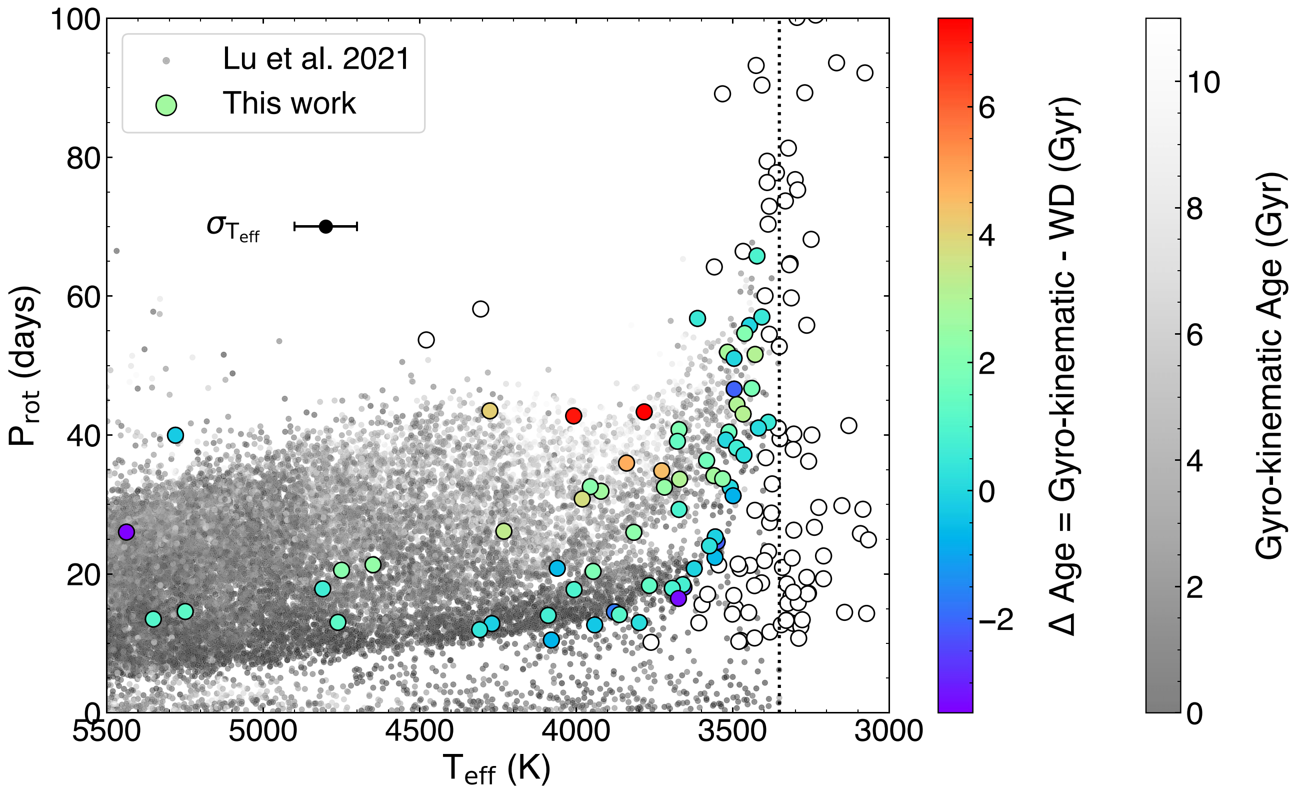

Figure 17. Kepler stars are color coded by their gyro-kinematic ages (Y. L. Lu et al. 2021) in grays. The MS stars in our sample are plotted as larger circles and color coded by the difference between the median of the gyro-kinematic ages of the neighboring binned Kepler stars and the age inferred from the WD companions. The dashed vertical line shows the T_{eff} of the coolest star in the Kepler sample. MS stars for which age comparisons are not feasible due to an insufficient number of nearby Kepler stars are indicated with white circles. The typical uncertainty in T_{eff} is shown at the top.

Section 4.4.3. Furthermore, the MS stars populating the upper band of Figure 16 are distributed along the sharp rise in rotation period at the FCB and the disagreement between the WD and gyro-kinematic ages increases as we move toward longer periods, as shown in Figure 17. Therefore, gyro-kinematic ages, which assume that stars at similar periods and temperatures have the same ages, are likely not reliable for stars at the FCB.

Other factors that affect the precision of WD total ages are their mass and the IFMR. Precise mass measurements and well-constrained IFMRs are required to obtain precise ages of low-mass WDs ($M < 0.63\,M_{\odot}$) since their progenitor lifetimes represent a major part of their total age. However, the WD companions of the MS stars in the upper band of Figure 17 are all high-mass WDs ($M > 0.67\,M_{\odot}$), which have short ZAMS progenitor lifetimes, and thus their age precision is not significantly affected by their mass and choice of IFMR. Furthermore, because formal age uncertainties of higher-mass WDs are often underestimated, we have applied inflation factors (T. M. Heintz et al. 2022). Lastly, the distribution of WD ages in our sample (gray histogram along the *x*-axis in Figure 16) more closely resembles that of the Kepler-APOGEE Cool Dwarfs sample (Z. R. Claytor et al. 2020) and Kepler field stars (V. Silva Aguirre et al. 2018). These age distributions peak at around 1–2 Gyr and do not exhibit the double peak observed in the gyro-kinematic age distribution (gray histogram along the *y*-axis in Figure 16).

The sharp increase of rotation periods at the FCB also challenges the hypothesis that the closing of the intermediate period gap detected in the Kepler distribution (A. McQuillan et al. 2014a) is caused by the disappearance of the radiative core, as proposed by Y. L. Lu et al. (2022). We argue instead that invoking the mechanics of core-envelope decoupling may not be necessary to produce a closure of the gap within the temperature range associated with the FCB. The steep incline of gyrochrones in the neighborhood of this boundary is such that a large range of rotational periods would be consistent with any single gyrochrone within this range of temperatures. This spread of permissible rotational periods is also far larger than the rotational-period separation between gyrochrones near the fully convective boundary, even for gyrochrones, which, at higher temperatures, would be separated by the intermediate period gap. This being the case, points on the period–temperature diagram drawn randomly from two such gyrochrones near the FCB would appear to overlap, thereby apparently closing the gap. This is true irrespective of the actual underlying physical origin for the gap to begin with. In turn, this may imply that we cannot interpret the closing of the intermediate period gap at this location as strong evidence for core-envelope decoupling, although the feature is still fundamentally tied to the loss of a radiative core.

4.5.2. *Gyro-kinematic Ages from Lu et al. (2023b)*

The shearing flows of the solar tachocline, the transition region between the convective zone and the underlying radiative core (J. Schou et al. 1998), are considered to play a key role in the process of magnetic field generation. Fully convective stars do not have a tachocline and therefore are expected to have a different dynamo mechanism. Recent observations of X-ray emissions from fully convective stars reveal that these stars host a dynamo with a rotation–activity relationship that closely resembles that of solar-like stars (N. J. Wright et al. 2018), implying that the presence of the tachocline may not be a critical factor in the creation of the stellar magnetic field. However, a recent work by Y. Lu et al. (2024b) suggested that the dynamos of partially and fully convective stars may be fundamentally different.

Using gyro-kinematic ages of a data set that combines the Kepler stars from Y. L. Lu et al. (2021) and stars with ZTF rotation periods from Y. L. Lu et al. (2022) and Y. Lu et al. (2024a), they found that fully convective stars exhibit a $1.51\times$ higher AM-loss rate than partially convective stars. To account for this, they suggest that fully convective stars necessitate a dipole field strength approximately 1.26 times greater, or a $1.44\times$ increase in the rate of mass loss, or a blend of both factors.

We use solar-metallicity tracks with $f_{\rm spot} = 0\%$ to compute the ratio of AM-loss rate of a $0.28\,M_\odot$ star and a $0.40\,M_\odot$ star at the same rotation period. We chose these masses to represent fully and partially convective stars, respectively, while also avoiding stars along the vertical feature in rotation period that we find at the FCB. For a range of rotation periods between 10 and 90 days, we find that the fully convective star always shows a higher AM-loss rate than the partially convective star by at least a factor of 2, except when its rotation period is shorter than 16 days. Therefore, we suggest that invoking a modification to the stellar dynamo mechanism is not necessary to explain the stronger magnetic braking at the FCB. By scaling the torque with Rossby number, our models naturally reproduce the sharp rise in rotation period at the FCB.

4.6. Activity Signatures

Because we are invoking changes in rotation period, Rossby number, and convective overturn timescales to explain the observed behavior, it is natural to ask whether there are observable activity signatures of such a physical transition.

Although the rotation periods increase across the fully convective boundary, the convective overturn timescales also increase, meaning that we expect very modest values of the Rossby number. Stars near the "spike" in the gyrochrones achieve Rossby numbers less than solar ($\sim$2) but greater than saturation ($\sim$0.1) despite the extremes they represent in both rotation period and convective overturn timescale. Rotation–activity correlations have emerged from a variety of activity signatures such as X-rays (N. J. Wright et al. 2011, 2018), Hα emission (E. R. Newton et al. 2017), and UV (K. France et al. 2018), and show that the activity level decreases with increasing rotation period and increases with decreasing Rossby number. If magnetic activity levels truly do track Rossby number, we expect these stars to be active, but neither unusually active nor unusually quiet compared to field stars of mixed ages at slightly hotter or slightly cooler temperatures.

In Figure 18 we show that stars "on the spike" do have Rossby numbers that are $\sim$0.2–0.7 lower than stars immediately hotter or cooler than the feature, depending on the age. If we assume, for example, that magnetic activity scales as Ro^{-2}, then this corresponds to a factor of $\sim$2–20 enhancement in activity for stars in a narrow mass range at the FCB. Observational $(L_X/L_{\rm bol})$–Ro relations display an order of magnitude of spread in the X-ray luminosities at fixed Rossby number, making the predicted activity signature at the FCB relatively subtle in comparison. Precision activity measurements in controlled environments like open clusters may represent the best hope of detecting an activity feature at the FCB.

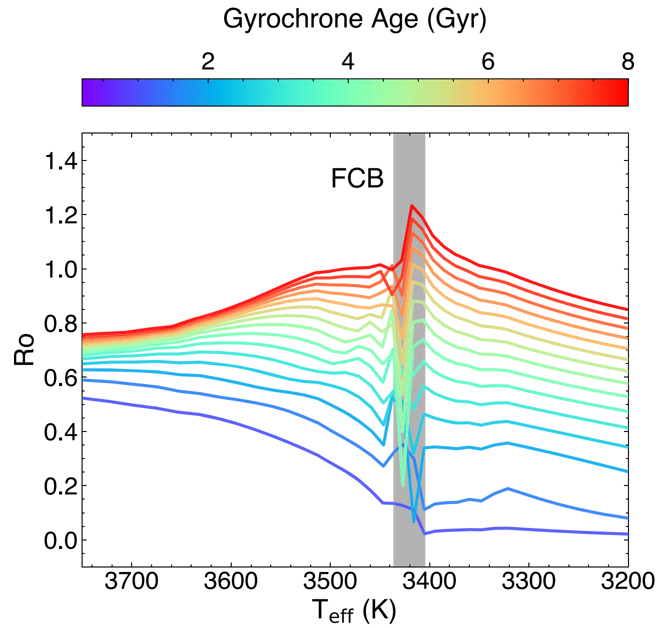

Figure 18. Rossby number as a function of effective temperature as shown by solar-metallicity, $f_{\rm spot} = 0\%$ gyrochrones color coded by their age. At the fully convective boundary, highlighted in gray, the Rossby number sees a sudden decrease followed by a sharp increase over the span of $\approx$50 K.

There have been observational efforts to examine the activity of stars in the vicinity of the FCB. W.-C. Jao et al. (2023) claim that stars above the observed M-dwarf luminosity gap (higher mass) are more active. By contrast, our models do not predict a lower Rossby number and higher activity rates just above the gap; instead, they predict that fully convective stars coolward (less massive) than the gap have lower Rossby numbers, and would thus appear more active (their long rotation periods are balanced by a larger τ_{cz}). Because existing field samples are relatively small and challenging to control for binarity, it is not yet obvious if this apparent tension is robust.

E. M. Boudreaux et al. (2024) similarly studied the activity of gap stars, finding that there was a larger scatter in both the observed rotation rates and activity levels on the cool (lower-mass) side of the gap. We create a simple stellar population where ages are drawn from a Gaussian centered on 3 Gyr with a width of 2 Gyr, truncated at 0 Gyr and 14 Gyr or the main-sequence turnoff age, whichever is younger for each mass in our model grid. In this toy model the dispersion in rotation periods does indeed increase across the FCB (by about a factor of 3 across the 100 K near the spike), as does the dispersion in predicted activity levels (again a factor $\sim$3 in $L_x/L_{\rm bol}$, assuming a Ro^{-2} scaling for activity proxies).

5. Conclusions

In this work, we constructed a sample of 185 wide, coeval WD + MS binaries with a measured rotation period for the MS companions, which are mostly K and M dwarfs. For the white dwarfs, we derived effective temperatures, surface gravities, and masses by fitting photometric data from various all-sky surveys with atmosphere models—either hydrogen dominated, pure helium, or mixed—depending on the spectral classification available for each white dwarf. Using these atmospheric parameters, we computed the total age of each WD using WD cooling models, a theoretically motivated and observationally calibrated IFMR, and stellar evolution model grids. Our sample is dominated by massive ($M > 0.67\,M_{\odot}$) WDs for which the total age is primarily governed by cooling processes. This allowed us to achieve an average uncertainty of 10% on the WD total age.

To model the rotational evolution of the MS stars, we adopted an angular momentum–loss prescription for magnetized winds from J. L. van Saders & M. H. Pinsonneault (2013) and modeled the internal angular momentum transport as in the standard two-zone model from P. A. Denissenkov et al. (2010). We calibrated gyrochronology models to reproduce the rotational sequences of the open clusters Pleiades, Praesepe, NGC 6811, Ruprecht 147, NGC 6819, and M67 and the rotation period of the Sun at solar age. We used the calibrated gyrochrones to predict the rotation periods of the MS stars in the sample given their effective temperature and the age from their WD companions.

We find that the rotation period steeply increases across a narrow temperature range for stars near the FCB and up to $\sim$8 Gyr. This sharp rise in rotation period is evident in both the models and the data and suggests that stars rotating slowly at the FCB are not necessarily old.

We propose that the rise in rotation period at this boundary is driven by an increase in convective overturn timescale due to structural differences between partially and fully convective stars. As the convective envelope extends deeper into the star, encompassing a larger fraction of the overall stellar mass, it results in a rise in the pressure scale height and a reduction in convective velocity, leading to an increase in τ_{cz}. Furthermore, we argue that the sharpness of such rise in τ_{cz} is induced by nonequilibrium ^{3}He burning occurring for stars just short of the FCB (J. L. van Saders & M. H. Pinsonneault 2012a). Although the exact location of this vertical feature in τ_{cz}, and consequently $P_{\rm rot}$, depends on properties like metallicity, spot covering fraction, and τ_{cz} prescriptions, the existence of this feature does not.

Due to the current uncertainties in temperature measurements, the rotation periods of stars situated along this distinct feature can be associated to a broad spectrum of gyrochrones, spanning a range of $\sim$6 Gyr. Consequently, despite gyrochronology being regarded as a promising approach for determining the ages of low-mass stars, our findings suggest that age estimation via this method might pose greater challenges when applied to stars located at the FCB.

Future work is planned to obtain spot covering fractions for the MS stars in our sample to allow for a better comparison between the observed and the model rotation periods. Furthermore, as discussed in Section 4, metallicity has a nonnegligible impact on stellar spindown, and therefore more robust predictions of rotation period will be achieved by taking into account the inherent variability and uncertainty associated with this parameter in our models. Having metallicity values for more stars in our sample would also allow for more accurate comparison between the observed and model rotation periods as well as better WD age estimates, since the IMFR is likely to be sensitive to the metallicity of the progenitor stars (J. D. Cummings et al. 2019). Knowing the metallicity of some of the WDs in the sample will be useful to refine the IFMRs and obtain even more precise WD ages (R. Raddi et al. 2022). Thus, these systems represent optimal targets for wide-field spectroscopic surveys. For example, the Milky Way Mapper of the Sloan Digital Sky Survey V (J. A. Kollmeier et al. 2017) is collecting APOGEE infrared spectra for 6 million stars across the entire Milky Way and will provide metallicities for all these stars.

Having kinematic ages that remain unaffected by the rotation of main-sequence stars would be advantageous. Such ages could serve as a supplementary assessment for the rapid increase in rotation period observed at the FCB. Furthermore, they have the potential to offer insights into the underlying causes of the discordance observed between the gyro-kinematic ages detailed in Y. L. Lu et al. (2021) and the ages deduced from our WD sample.

Finally, our sample represents a subset drawn from a pool of 5005 WD + MS binary systems with measured rotation periods. It is worth noting that there exists a total of 22,563 such systems (K. El-Badry et al. 2021). Access to a greater number of rotation periods would prove invaluable in expanding our sample size, probing even older age ranges, and enhancing our understanding of the rotational evolution of low-mass stars. While the count of TESS-derived rotation periods for cool, MS stars through machine learning techniques is on the rise (Z. R. Claytor et al. 2024), there is also promise in forthcoming space missions like the Nancy Grace Roman Space Telescope (D. Spergel et al. 2015), which will enable many new rotation-period measurements.

Acknowledgments

We thank the anonymous referees for the careful review and valuable feedback, which greatly improved the quality of this manuscript. We would like to thank Dhvanil Desai, Zachary Claytor, Lyra Cao, and Nicholas Saunders for helpful discussions. We acknowledge support from the National Science Foundation under grants No. AST-1908119 and AST-1908723. JMJO acknowledges support from NASA through the NASA Hubble Fellowship grant HST-HF2-51517.001, awarded by STScI, which is operated by the Association of Universities for Research in Astronomy, Incorporated, under NASA contract NAS5-26555.

Appendix A
Supporting Figures for Section 4.3

Figures 19 and 20 show that the formation of the spike in $P_{\rm rot}$ at the fully convective boundary is caused by an increase in $\tau_{\rm cz}$ due to internal structural changes between partially and fully convective stars.

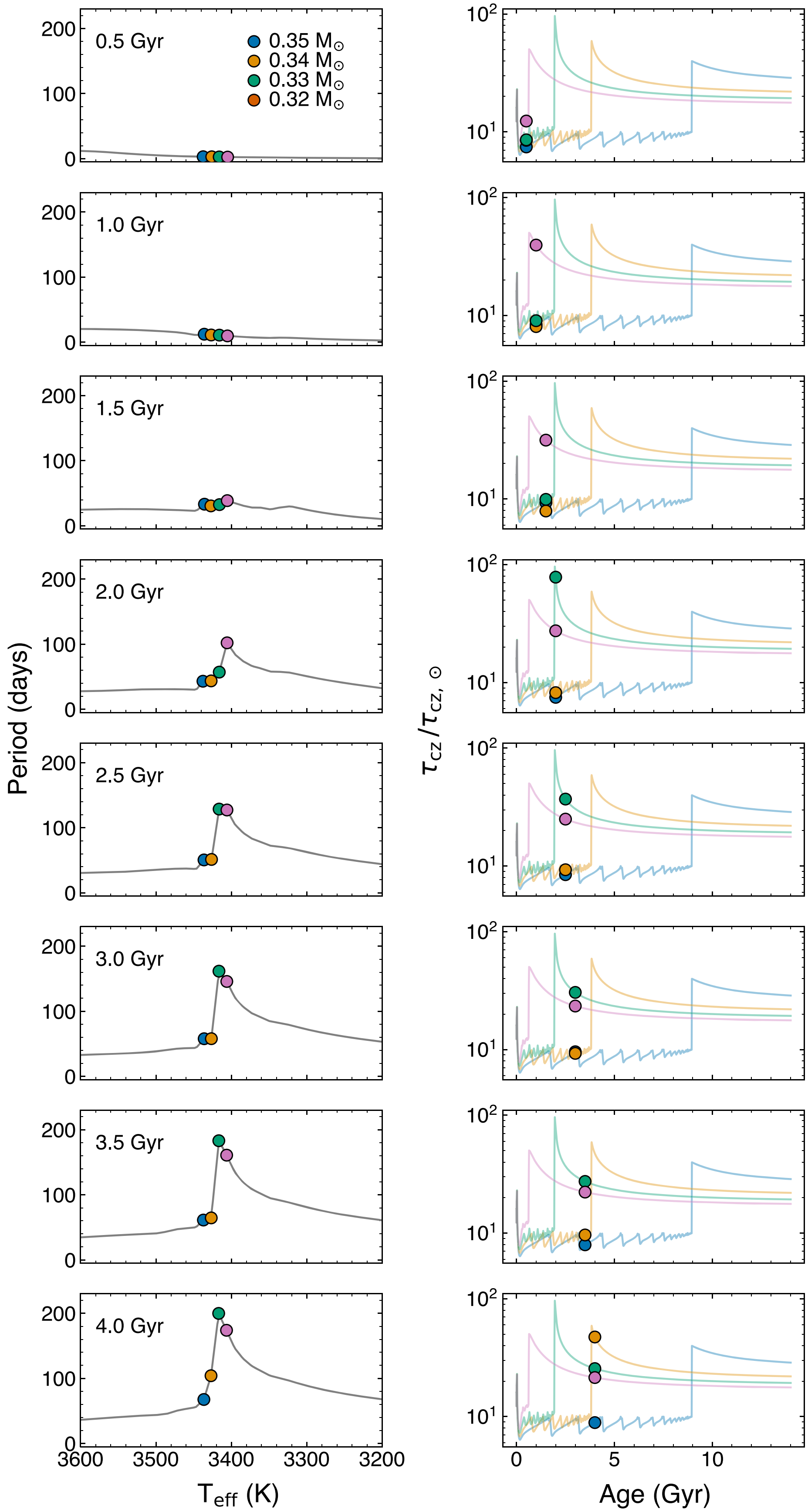

Figure 19. Left: rotation period as a function of effective temperature for a specific age, computed using a solar-metallicity model grid with $f_{\rm spot} = 0\%$. Gray solid lines represent gyrochrones. Markers indicate stars undergoing nonequilibrium ^{3}He burning. Right: the convective overturn timescale, normalized by the solar value, as a function of age for the same stars. Markers display τ_{cz} at the corresponding ages shown in the left plots. The saw-toothed curves represent fully convective episodes. The jump in τ_{cz} from the saw-toothed to the smooth curve marks the transition to a fully convective state. Once the stars become fully convective, they reach the peak of the $P_{\rm rot}$ spike in the plot on the left.

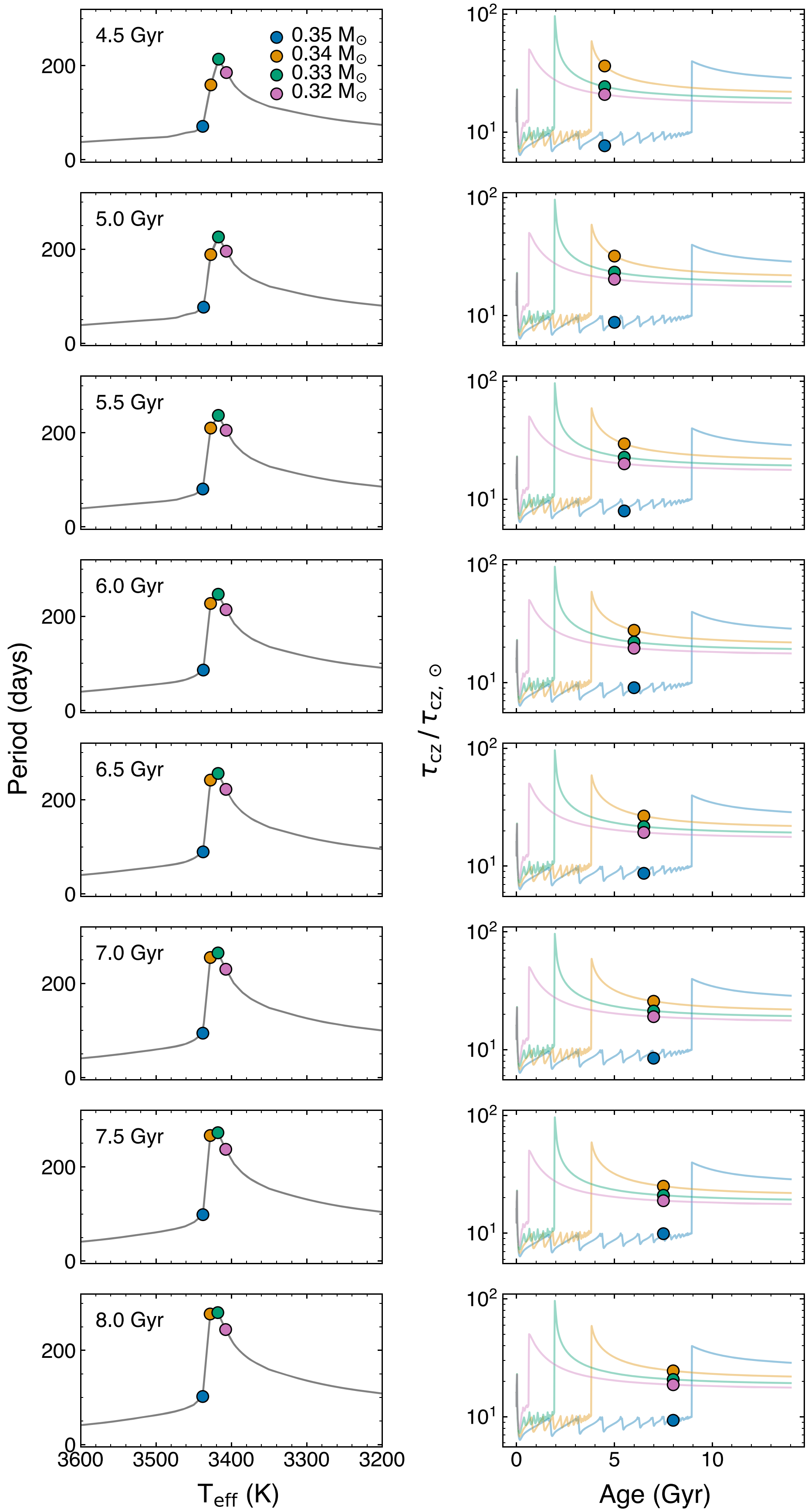

Figure 20. Same as in Figure 19 but extended to older ages.

Appendix B
Data Sample

Properties of the MS + WD sample used in this work are reported in Table 1. The table lists the Gaia DR3 IDs, effective temperatures, observed surface rotation periods of the MS stars, WD surface gravities, the computed WD total ages and WD spectral types.

Table 1
Sample of 185 MS + WD Wide Binaries and Their Properties

MS Gaia DR3 ID	WD Gaia DR3 ID	MS $T_{\rm eff}$ (K)	MS $P_{\rm rot}$ (days)	WD $T_{\rm eff}$ (K)	WD log(g) (dex)	WD Total Age (Gyr)	WD Spectral Type
18493721155296640	18493721155296768	3316	64.7	$13,230^{+200}_{-200}$	$8.09^{+0.04}_{-0.04}$	$1.09^{+0.18}_{-0.12}$	DA (1)
28185744355533824	28185744355056128	3371	116.3	9120^{+60}_{-520}	$8.47^{+0.26}_{-0.28}$	$2.01^{+0.41}_{-0.25}$	…
52639226555782656	52639153540042496	3921	31.9	6590^{+230}_{-250}	$8.28^{+0.08}_{-0.08}$	$3.73^{+0.28}_{-0.20}$	…
77783305135054720	77782544925602432	3249	68.2	6270^{+80}_{-90}	$8.16^{+0.04}_{-0.04}$	$3.49^{+0.25}_{-0.20}$	…
85649623637225856	85649413183595392	3129	41.4	6480^{+130}_{-140}	$8.25^{+0.05}_{-0.05}$	$3.70^{+0.19}_{-0.14}$	DA (2)
115344202888681216	115344095513403520	3558	64.2	6220^{+110}_{-110}	$8.31^{+0.04}_{-0.04}$	$4.49^{+0.11}_{-0.10}$	DA (2)
166587938734739456	166587938734739328	3225	29.6	9130^{+170}_{-170}	$8.25^{+0.04}_{-0.04}$	$1.52^{+0.05}_{-0.05}$	DA (2)
181306276262296192	181306168886213120	3761	10.2	7180^{+350}_{-380}	$8.23^{+0.11}_{-0.11}$	$2.63^{+0.36}_{-0.31}$	…
192005963220544768	192005967510846848	3287	137.2	$11,830^{+520}_{-630}$	$8.16^{+0.06}_{-0.06}$	$0.99^{+0.21}_{-0.10}$	DA (2)
196589900204859392	196589861548739584	4060	20.8	6720^{+200}_{-220}	$8.34^{+0.07}_{-0.07}$	$3.88^{+0.20}_{-0.14}$	…
267776887192982784	267777604451603328	3429	29.2	7220^{+160}_{-170}	$8.50^{+0.04}_{-0.05}$	$3.95^{+0.07}_{-0.05}$	DA (2)
268123027195914368	268123332136902016	3128	200.0	9180^{+260}_{-270}	$8.36^{+0.05}_{-0.05}$	$1.57^{+0.08}_{-0.06}$	DQ (2)
271639471546035584	271639432884899712	3446	55.8	6770^{+240}_{-260}	$8.28^{+0.08}_{-0.08}$	$3.47^{+0.27}_{-0.19}$	…
293717390146554624	293717454571113984	4058	169.2	7810^{+280}_{-320}	$8.21^{+0.08}_{-0.09}$	$2.06^{+0.24}_{-0.14}$	…
348345663302119936	348345659004467840	3223	144.9	6640^{+120}_{-120}	$8.22^{+0.04}_{-0.04}$	$3.27^{+0.17}_{-0.16}$	DA (2)
374254624016996352	374254619721557504	4269	12.8	9860^{+250}_{-240}	$8.50^{+0.05}_{-0.04}$	$1.41^{+0.33}_{-0.12}$	DC (2)
377335386879208704	377335451303175808	3955	32.6	5970^{+90}_{-90}	$8.20^{+0.04}_{-0.04}$	$4.26^{+0.23}_{-0.19}$	…
390689402277884544	390689397980291072	3532	89.1	7140^{+150}_{-150}	$8.28^{+0.04}_{-0.04}$	$2.94^{+0.13}_{-0.13}$	DA (2)
395377200164554368	395377513698597888	3142	14.5	6000^{+90}_{-90}	$8.33^{+0.04}_{-0.04}$	$5.09^{+0.08}_{-0.07}$	DA (2)
395932320399086464	395932247377032320	4308	12.0	$11,250^{+560}_{-680}$	$8.20^{+0.09}_{-0.08}$	$1.03^{+0.20}_{-0.10}$	…
411948871922982528	411951822555835648	3598	15.6	8300^{+330}_{-350}	$8.33^{+0.08}_{-0.08}$	$2.07^{+0.13}_{-0.17}$	DA (2)
420483143738322304	420483139441443200	3474	10.4	8790^{+460}_{-520}	$8.23^{+0.12}_{-0.12}$	$1.62^{+0.35}_{-0.12}$	…
506944889856368256	506944889847883008	3671	40.8	6820^{+230}_{-260}	$8.18^{+0.08}_{-0.08}$	$2.80^{+0.45}_{-0.28}$	…
544555471783803136	544555467486553984	4079	10.5	7670^{+260}_{-280}	$8.24^{+0.08}_{-0.08}$	$2.21^{+0.16}_{-0.17}$	…
545940409758573824	545940164944375296	3512	40.4	7360^{+140}_{-140}	$8.23^{+0.04}_{-0.04}$	$2.44^{+0.11}_{-0.11}$	DA (2)
546388323308593280	546388319012071040	3263	19.5	6260^{+90}_{-90}	$8.22^{+0.04}_{-0.04}$	$3.85^{+0.20}_{-0.18}$	…
549835601498785536	549788563014393728	3521	39.3	6270^{+110}_{-120}	$8.20^{+0.05}_{-0.05}$	$3.73^{+0.24}_{-0.20}$	DA (2)
564321564114510080	564509271364217344	3425	93.2	8480^{+240}_{-250}	$8.30^{+0.06}_{-0.06}$	$1.85^{+0.08}_{-0.09}$	DA (2)
569795207875481344	569795203578976128	3383	72.9	5470^{+70}_{-70}	$8.14^{+0.04}_{-0.04}$	$5.45^{+0.31}_{-0.18}$	…
583948877461123584	583949251122623232	3466	66.4	7480^{+100}_{-100}	$8.13^{+0.04}_{-0.04}$	$2.23^{+0.25}_{-0.10}$	DA (3)
594439627139102720	594439519764767232	4761	13.0	$20,450^{+1030}_{-1000}$	$8.20^{+0.04}_{-0.04}$	$0.53^{+0.12}_{-0.06}$	DBA (4)
642837139695905024	642837135401004672	3439	46.7	6970^{+80}_{-80}	$8.13^{+0.04}_{-0.04}$	$2.58^{+0.18}_{-0.10}$	DA (5)
657819944131129472	657820012850606080	3487	38.1	9040^{+130}_{-140}	$8.29^{+0.04}_{-0.04}$	$1.63^{+0.15}_{-0.08}$	DB (4)
678153006506212480	678153006506212608	3390	79.4	$15,060^{+730}_{-710}$	$8.50^{+0.05}_{-0.05}$	$0.60^{+0.06}_{-0.04}$	…
692919207148481920	692919202851887104	3311	130.4	5820^{+70}_{-70}	$8.11^{+0.04}_{-0.04}$	$4.18^{+0.55}_{-0.31}$	DA (2)
701860809365640704	701860809367120640	3491	15.0	$19,890^{+440}_{-530}$	$8.48^{+0.08}_{-0.08}$	$0.35^{+0.08}_{-0.05}$	…
719440149164429824	719439423313644672	3381	11.6	7640^{+110}_{-110}	$8.25^{+0.04}_{-0.04}$	$2.24^{+0.30}_{-0.10}$	DQ (5)
739321307963291136	739321312258441216	3314	16.8	$10,230^{+380}_{-420}$	$8.41^{+0.07}_{-0.07}$	$1.35^{+0.05}_{-0.08}$	…
748247452595214336	748247456890075136	3092	25.8	6350^{+80}_{-80}	$8.16^{+0.04}_{-0.04}$	$3.38^{+0.21}_{-0.17}$	…
765964300065414144	765965051684223360	3396	60.0	5980^{+70}_{-70}	$8.12^{+0.04}_{-0.04}$	$3.85^{+0.30}_{-0.20}$	DA (2)
793941132918315392	793917660919464960	3816	26.0	8950^{+240}_{-250}	$8.33^{+0.06}_{-0.06}$	$1.68^{+0.06}_{-0.06}$	…
821363846267866368	821363807610959104	3351	52.7	6920^{+110}_{-110}	$8.25^{+0.04}_{-0.04}$	$3.03^{+0.15}_{-0.12}$	…
823582763810855168	823582759515662592	3549	24.6	6520^{+140}_{-150}	$8.20^{+0.06}_{-0.06}$	$3.33^{+0.30}_{-0.26}$	…
844085460212939392	844085490277157376	3726	34.8	$22,660^{+1960}_{-1020}$	$8.21^{+0.05}_{-0.05}$	$0.43^{+0.06}_{-0.05}$	DA (2)
851088662087300992	851088662087301120	3612	56.8	5460^{+70}_{-70}	$8.10^{+0.04}_{-0.04}$	$5.37^{+0.56}_{-0.35}$	DA (2)
855190699452263040	855190695156439680	3210	19.3	5830^{+70}_{-70}	$8.15^{+0.04}_{-0.04}$	$4.28^{+0.23}_{-0.18}$	DA (2)
856837802230613504	856837729215097984	4008	42.7	$12,890^{+580}_{-660}$	$8.18^{+0.05}_{-0.05}$	$0.86^{+0.14}_{-0.07}$	…
860411043221913984	860411038927355264	3623	20.8	9250^{+270}_{-290}	$8.25^{+0.07}_{-0.07}$	$1.48^{+0.10}_{-0.07}$	…
861184515292492288	861184515291473536	3239	26.7	5300^{+60}_{-60}	$8.13^{+0.04}_{-0.04}$	$6.31^{+0.47}_{-0.23}$	DZ (2)
861951493372439424	861951489076842880	3341	20.9	7040^{+120}_{-120}	$8.13^{+0.05}_{-0.05}$	$2.52^{+0.45}_{-0.16}$	…
873994719110827136	873994719110827264	3326	18.6	7600^{+90}_{-90}	$8.37^{+0.04}_{-0.04}$	$2.27^{+0.37}_{-0.11}$	DC (6)

Table 1
(Continued)

MS Gaia DR3 ID	WD Gaia DR3 ID	MS $T_{\rm eff}$ (K)	MS $P_{\rm rot}$ (days)	WD $T_{\rm eff}$ (K)	WD log(g) (dex)	WD Total Age (Gyr)	WD Spectral Type
889041879334169344	889041668879549696	3655	18.1	6660^{+200}_{-220}	$8.31^{+0.07}_{-0.08}$	$3.81^{+0.24}_{-0.18}$	⋯
896972484905743872	898473932456801024	3304	40.1	9300^{+130}_{-120}	$8.43^{+0.04}_{-0.04}$	$1.55^{+0.16}_{-0.08}$	DC (6)
909162529804018688	909162525508848000	3258	17.2	$10,430^{+190}_{-190}$	$8.38^{+0.04}_{-0.04}$	$1.26^{+0.02}_{-0.02}$	DA (2)
909192835093328896	909192830801295104	3324	15.8	6280^{+70}_{-70}	$8.10^{+0.04}_{-0.04}$	$3.36^{+0.40}_{-0.26}$	DA (2)
931487529290752000	931487524994983808	3486	44.4	8090^{+120}_{-130}	$8.09^{+0.04}_{-0.04}$	$2.12^{+0.49}_{-0.27}$	DA (6)
990883830321907456	990883830322597376	3409	120.0	$10,560^{+240}_{-250}$	$8.52^{+0.04}_{-0.04}$	$1.25^{+0.03}_{-0.03}$	DC (2)
991811169597579520	991811165304213760	3331	73.7	8480^{+140}_{-140}	$8.15^{+0.04}_{-0.04}$	$1.73^{+0.17}_{-0.10}$	DA (2)
1018436324699616000	1018436320403748480	3556	22.4	8810^{+140}_{-140}	$8.35^{+0.04}_{-0.04}$	$1.83^{+0.06}_{-0.05}$	DAH (7)
1036217489305134848	1036217489305134976	3290	15.9	8760^{+130}_{-130}	$8.16^{+0.04}_{-0.04}$	$1.63^{+0.10}_{-0.08}$	DA (2)
1055800238072103296	1055800165056700416	3234	100.5	5970^{+70}_{-80}	$8.15^{+0.04}_{-0.04}$	$4.00^{+0.27}_{-0.21}$	DA (2)
1103650292622702976	1103650292623968640	3555	25.3	9690^{+450}_{-520}	$8.22^{+0.11}_{-0.11}$	$1.33^{+0.31}_{-0.11}$	DA (2)
1175151533777264256	1175151538072196992	3422	65.8	7820^{+120}_{-130}	$8.20^{+0.04}_{-0.04}$	$2.04^{+0.10}_{-0.07}$	DA (2)
1202830540713288064	1202830540713287936	3386	41.8	$10,850^{+240}_{-250}$	$8.22^{+0.04}_{-0.04}$	$1.09^{+0.05}_{-0.04}$	DA (5)
1214994506568260608	1214994502274335360	3495	46.6	5820^{+90}_{-100}	$8.67^{+0.04}_{-0.04}$	$6.71^{+0.24}_{-0.26}$	⋯
1222565537480885376	1222565533185185024	3353	177.6	5900^{+70}_{-70}	$8.14^{+0.04}_{-0.04}$	$4.06^{+0.35}_{-0.22}$	DA (2)
1233273646861764480	1233273646861782656	3360	77.8	9350^{+320}_{-330}	$8.47^{+0.07}_{-0.06}$	$1.90^{+0.13}_{-0.11}$	⋯
1291263917336163456	1291263913040087936	3407	18.7	7040^{+80}_{-80}	$8.13^{+0.04}_{-0.04}$	$2.52^{+0.20}_{-0.10}$	DA (3)
1299293685113944448	1299293680818146176	3300	76.8	6310^{+90}_{-90}	$8.19^{+0.04}_{-0.04}$	$3.60^{+0.22}_{-0.18}$	DA (2)
1319540848141886976	1319540843845667072	4479	53.7	9860^{+300}_{-300}	$8.16^{+0.07}_{-0.06}$	$1.33^{+0.29}_{-0.12}$	⋯
1322796261553157760	1322796261553165824	3798	13.0	$11,700^{+180}_{-180}$	$8.13^{+0.04}_{-0.04}$	$1.06^{+0.11}_{-0.05}$	DA (8)
1332138536976820096	1332138532682327552	3445	21.2	7360^{+150}_{-160}	$8.16^{+0.05}_{-0.05}$	$2.29^{+0.25}_{-0.13}$	⋯
1340289109302083584	1340289113593902080	3257	36.2	9110^{+200}_{-210}	$8.33^{+0.05}_{-0.04}$	$1.62^{+0.04}_{-0.04}$	⋯
1341558083155952512	1341557984372129536	3263	55.8	7340^{+110}_{-120}	$8.29^{+0.04}_{-0.04}$	$2.77^{+0.11}_{-0.12}$	DA (4)
1342071937339096192	1342071933043493120	3269	89.3	6320^{+80}_{-90}	$8.24^{+0.04}_{-0.04}$	$3.92^{+0.16}_{-0.12}$	⋯
1345042955196670208	1345041748308955648	3260	17.1	5920^{+70}_{-70}	$8.16^{+0.04}_{-0.04}$	$4.14^{+0.18}_{-0.16}$	DA (2)
1355692412505713152	1355692408211800704	3659	18.5	$19,610^{+850}_{-890}$	$8.30^{+0.05}_{-0.05}$	$0.44^{+0.04}_{-0.03}$	DA (2)
1365015515194773632	1365015545259769600	3168	93.6	6430^{+120}_{-120}	$8.28^{+0.04}_{-0.04}$	$3.99^{+0.14}_{-0.12}$	DA (2)
1410448641324559744	1410448259071414528	3209	130.4	8360^{+110}_{-100}	$8.32^{+0.04}_{-0.04}$	$1.88^{+0.11}_{-0.07}$	DQ (3)
1412158789927363328	1412158789927364224	3480	10.3	$16,680^{+1030}_{-1050}$	$8.25^{+0.07}_{-0.07}$	$0.57^{+0.09}_{-0.06}$	⋯
1444236977242948480	1444236972948340480	3583	36.3	7610^{+230}_{-260}	$8.17^{+0.08}_{-0.08}$	$2.14^{+0.51}_{-0.16}$	⋯
1444622768385439232	1444622768385439104	3322	81.3	8650^{+120}_{-110}	$8.33^{+0.04}_{-0.04}$	$1.75^{+0.10}_{-0.06}$	DQ (5)
1526498829461895936	1526498863822158592	3345	12.7	7890^{+90}_{-100}	$8.32^{+0.04}_{-0.04}$	$2.37^{+0.07}_{-0.07}$	DA (3)
1541905598706074880	1541905560050370816	3496	16.9	$18,950^{+250}_{-330}$	$8.35^{+0.08}_{-0.07}$	$0.45^{+0.05}_{-0.06}$	⋯
1588270938897733888	1588270934604149632	3980	30.8	8700^{+260}_{-270}	$8.31^{+0.07}_{-0.07}$	$1.75^{+0.08}_{-0.09}$	⋯
1604198258179547264	1604200899583092992	3406	90.4	5610^{+70}_{-70}	$8.11^{+0.04}_{-0.04}$	$4.75^{+0.42}_{-0.24}$	DA (2)
1659015063216647296	1659015063216647424	3318	64.5	8800^{+120}_{-130}	$8.10^{+0.04}_{-0.04}$	$1.78^{+0.42}_{-0.19}$	DA (3)
1681875731024076160	1681875726730147968	3430	102.0	8900^{+180}_{-190}	$8.28^{+0.05}_{-0.05}$	$1.63^{+0.06}_{-0.05}$	⋯
1748817160020646784	1748816983925915776	5280	40.0	5890^{+70}_{-70}	$8.09^{+0.04}_{-0.04}$	$4.06^{+0.27}_{-0.20}$	DA (8)
1766826194114207360	1766826194114406656	4649	21.3	$13,320^{+470}_{-480}$	$8.33^{+0.04}_{-0.04}$	$0.77^{+0.03}_{-0.03}$	DZA (10)
1787683727830825856	1787683723535019776	3477	20.8	6440^{+90}_{-90}	$8.15^{+0.04}_{-0.04}$	$3.17^{+0.25}_{-0.16}$	DA (2)
1803336714670003840	1803336749029801728	4231	26.1	$15,410^{+500}_{-540}$	$8.13^{+0.04}_{-0.04}$	$0.76^{+0.18}_{-0.09}$	⋯
1812554680855696896	1812554676560349568	3478	292.4	$16,227^{+690}_{-770}$	$8.36^{+0.05}_{-0.05}$	$0.56^{+0.03}_{-0.03}$	DA (2)
1819001289330307200	1819001289323819520	3507	32.4	9600^{+490}_{-540}	$8.32^{+0.10}_{-0.10}$	$1.42^{+0.11}_{-0.08}$	⋯
1822194099312577024	1822193996219126784	3312	59.7	6500^{+100}_{-100}	$8.18^{+0.04}_{-0.04}$	$3.26^{+0.16}_{-0.15}$	DA (2)
1830600484179388416	1830600484161582464	3693	17.9	$17,700^{+1750}_{-1090}$	$8.59^{+0.10}_{-0.10}$	$0.44^{+0.07}_{-0.05}$	⋯
1874965739686844032	1874965499168713600	3878	14.5	7120^{+100}_{-100}	$8.33^{+0.04}_{-0.04}$	$3.25^{+0.10}_{-0.08}$	DA (2)
1880373172232064256	1880373172233144192	3483	21.4	$19,500^{+710}_{-760}$	$8.29^{+0.04}_{-0.04}$	$0.45^{+0.04}_{-0.03}$	DA (2)
1911106416309693952	1911106416309735552	3072	14.3	$11,750^{+350}_{-370}$	$8.46^{+0.04}_{-0.04}$	$1.02^{+0.04}_{-0.05}$	DA (2)
1937074166540526976	1937827194563435648	3516	51.9	9010^{+160}_{-160}	$8.22^{+0.04}_{-0.04}$	$1.78^{+0.49}_{-0.18}$	DQ (2)
1969985710668480256	1969985710668477184	3285	143.5	$10,280^{+500}_{-560}$	$8.64^{+0.08}_{-0.08}$	$1.96^{+0.06}_{-0.05}$	⋯
1996725077535282944	1996725077535283200	3632	104.1	5500^{+70}_{-70}	$8.08^{+0.04}_{-0.04}$	$5.27^{+0.36}_{-0.27}$	DA (8)
2010645375776770304	2010692306878145280	3448	14.4	$24,610^{+860}_{-870}$	$8.38^{+0.04}_{-0.04}$	$0.32^{+0.02}_{-0.04}$	DA (2)
2018812170226865664	2018818045723591680	3941	12.7	$10,660^{+630}_{-700}$	$8.37^{+0.10}_{-0.09}$	$1.19^{+0.07}_{-0.09}$	DA (2)
2020837264488052864	2020837157077399552	4749	20.5	9590^{+240}_{-210}	$8.39^{+0.04}_{-0.04}$	$1.47^{+0.17}_{-0.10}$	DC (2)
2048599211506044160	2048599314570668544	3839	36.0	7320^{+170}_{-160}	$8.39^{+0.05}_{-0.05}$	$2.44^{+0.32}_{-0.13}$	DC (2)
2053240524958351360	2053240524960871680	3417	41.0	9400^{+170}_{-180}	$8.16^{+0.04}_{-0.04}$	$1.43^{+0.11}_{-0.08}$	DA (2)
2053585565450552960	2053584770878226304	5351	13.5	$14,350^{+500}_{-500}$	$8.43^{+0.04}_{-0.04}$	$0.68^{+0.03}_{-0.05}$	DA (2)

Table 1
(Continued)

MS Gaia DR3 ID	WD Gaia DR3 ID	MS $T_{\rm eff}$ (K)	MS $P_{\rm rot}$ (days)	WD $T_{\rm eff}$ (K)	WD log(g) (dex)	WD Total Age (Gyr)	WD Spectral Type
2067604574919660416	2067604574919660544	3310	22.3	$10,350^{+510}_{-590}$	$8.25^{+0.10}_{-0.10}$	$1.18^{+0.16}_{-0.08}$	⋯
2069622492291282176	2069622487994113408	3580	17.1	$19,430^{+600}_{-620}$	$8.36^{+0.04}_{-0.04}$	$0.43^{+0.02}_{-0.02}$	DA (2)
2080422720138489344	2080422720133121152	3798	163.1	7040^{+190}_{-210}	$8.19^{+0.07}_{-0.07}$	$2.60^{+0.28}_{-0.23}$	DA (2)
2141224751076269824	2141224781139309312	3307	12.9	5480^{+90}_{-90}	$8.12^{+0.05}_{-0.05}$	$5.26^{+1.17}_{-0.33}$	⋯
2142368311889141248	2142368346248880896	3430	10.8	7330^{+240}_{-260}	$8.27^{+0.07}_{-0.08}$	$2.66^{+0.22}_{-0.22}$	⋯
2187901837176956800	2187901832880159488	3498	31.3	8260^{+250}_{-270}	$8.34^{+0.07}_{-0.07}$	$2.15^{+0.13}_{-0.17}$	⋯
2187942828344053888	2187942789690550272	3390	76.4	9610^{+530}_{-600}	$8.43^{+0.11}_{-0.11}$	$1.63^{+0.12}_{-0.17}$	⋯
2205790165505947392	2205790169802867200	3349	39.5	6640^{+220}_{-240}	$8.17^{+0.09}_{-0.09}$	$3.00^{+0.64}_{-0.34}$	⋯
2238010155466716544	2238010185526881792	3382	27.4	6890^{+120}_{-120}	$8.19^{+0.04}_{-0.04}$	$2.73^{+0.15}_{-0.16}$	⋯
2255996069750790528	2255996069748606976	3544	21.3	6070^{+120}_{-130}	$8.23^{+0.05}_{-0.05}$	$4.32^{+0.25}_{-0.19}$	⋯
2275852459474001664	2275852455177465088	3376	28.8	7960^{+220}_{-230}	$8.41^{+0.06}_{-0.06}$	$2.77^{+0.13}_{-0.11}$	DA (2)
2299189284536000256	2299190006090503808	3501	14.2	$17,890^{+520}_{-550}$	$8.30^{+0.04}_{-0.04}$	$0.49^{+0.02}_{-0.02}$	DA (8)
2508478574102156544	2508478569806892928	3328	13.4	7470^{+160}_{-170}	$8.32^{+0.05}_{-0.05}$	$2.79^{+0.16}_{-0.13}$	⋯
2512689428758531456	2512689424463488256	3671	29.3	8490^{+240}_{-260}	$8.51^{+0.06}_{-0.06}$	$2.69^{+0.10}_{-0.06}$	⋯
2519281859960487424	2519281855665451008	3292	75.3	6890^{+100}_{-100}	$8.26^{+0.04}_{-0.04}$	$3.16^{+0.14}_{-0.11}$	⋯
2539792321663876736	2539792317371533440	3329	13.3	9310^{+460}_{-490}	$8.25^{+0.11}_{-0.11}$	$1.46^{+0.20}_{-0.10}$	⋯
2576762025758278656	2576762266276447104	4089	14.0	$14,370^{+370}_{-370}$	$8.25^{+0.04}_{-0.04}$	$0.69^{+0.03}_{-0.03}$	DA (2)
2579247712310922240	2579247708016296448	3430	18.3	7060^{+220}_{-260}	$8.19^{+0.08}_{-0.09}$	$2.57^{+0.40}_{-0.26}$	⋯
2656915701868610944	2656915697573351680	3466	43.0	9320^{+200}_{-210}	$8.32^{+0.04}_{-0.04}$	$1.52^{+0.04}_{-0.04}$	⋯
2700089675200729216	2700089675200402048	3208	108.4	5770^{+100}_{-100}	$8.21^{+0.05}_{-0.05}$	$4.83^{+0.25}_{-0.21}$	⋯
2724335723363858944	2724335723364297344	3282	12.4	9160^{+230}_{-260}	$8.30^{+0.05}_{-0.06}$	$1.55^{+0.07}_{-0.05}$	⋯
2739560214200407168	2739560218493488512	3669	33.6	$12,010^{+600}_{-700}$	$8.20^{+0.07}_{-0.07}$	$0.93^{+0.15}_{-0.09}$	⋯
2781085405419253504	2781085401124115328	3454	159.7	6490^{+80}_{-80}	$8.18^{+0.04}_{-0.04}$	$3.36^{+0.45}_{-0.19}$	DZ (6)
2816359731303136384	2816359727009816960	3151	29.8	5230^{+60}_{-60}	$8.21^{+0.04}_{-0.04}$	$7.46^{+0.15}_{-0.10}$	⋯
2824510273561942272	2824510239202203392	3373	33.0	7590^{+150}_{-150}	$8.21^{+0.04}_{-0.04}$	$2.20^{+0.11}_{-0.08}$	⋯
2857544378863193472	2857547329505058176	3304	159.0	6010^{+70}_{-70}	$8.16^{+0.04}_{-0.04}$	$3.94^{+0.17}_{-0.15}$	DA (2)
2858833212649253504	2858833208354052096	3495	51.0	5810^{+70}_{-70}	$8.18^{+0.04}_{-0.04}$	$4.52^{+0.18}_{-0.15}$	DA (2)
3047076750159238016	3047076750150944512	3597	270.4	5890^{+170}_{-180}	$8.29^{+0.09}_{-0.09}$	$5.05^{+0.33}_{-0.20}$	⋯
3096007732007670144	3096007762070816128	3862	14.1	$23,110^{+1070}_{-1870}$	$8.20^{+0.05}_{-0.05}$	$0.45^{+0.11}_{-0.05}$	DB (5)
3137340435682881920	3137340435679753728	3766	18.3	$22,880^{+3860}_{-3230}$	$9.12^{+0.15}_{-0.11}$	$0.52^{+0.08}_{-0.13}$	⋯
3145894292546764544	3145894288249489152	3385	23.2	8060^{+230}_{-260}	$8.20^{+0.07}_{-0.07}$	$1.92^{+0.19}_{-0.10}$	⋯
3160143344767586176	3160143344767585536	3209	22.6	8520^{+280}_{-300}	$8.33^{+0.07}_{-0.07}$	$1.92^{+0.10}_{-0.13}$	⋯
3165392310198209664	3165392305902629504	3411	106.7	8830^{+150}_{-1560}	$8.56^{+0.04}_{-0.04}$	$2.62^{+0.04}_{-0.03}$	⋯
3235085949939746304	3235085949939746176	3077	92.1	5650^{+100}_{-100}	$8.14^{+0.05}_{-0.05}$	$4.69^{+0.60}_{-0.27}$	⋯
3238194445407460864	3238194372390557312	4305	58.1	7230^{+270}_{-290}	$8.30^{+0.09}_{-0.08}$	$2.92^{+0.28}_{-0.22}$	⋯
3276414466021403008	3276414466021403264	3194	111.1	7180^{+90}_{-90}	$8.42^{+0.04}_{-0.04}$	$2.65^{+0.18}_{-0.11}$	DC (11)
3278241888706974336	3278241888707395584	3196	117.5	6530^{+230}_{-240}	$8.21^{+0.08}_{-0.08}$	$3.33^{+0.39}_{-0.28}$	⋯
3283182338046329472	3283182265031074560	3306	17.4	9660^{+580}_{-640}	$8.38^{+0.12}_{-0.12}$	$1.50^{+0.10}_{-0.14}$	⋯
3317635947223274752	3317636703137518208	3317	125.4	6340^{+80}_{-80}	$9.29^{+0.04}_{-0.04}$	$3.99^{+0.08}_{-0.10}$	⋯
3361149463489086720	3361149527909420928	3354	41.0	9320^{+210}_{-220}	$8.53^{+0.04}_{-0.04}$	$2.13^{+0.06}_{-0.05}$	⋯
3369278874508583424	3369278767129521792	3673	16.5	6020^{+80}_{-80}	$8.23^{+0.04}_{-0.04}$	$4.40^{+0.14}_{-0.14}$	DA (2)
3369544303487186560	3369544234764481024	3278	13.4	5180^{+90}_{-100}	$8.12^{+0.06}_{-0.06}$	$7.07^{+1.89}_{-0.33}$	DA (2)
3387417517828617088	3387417513531897984	3428	51.6	9660^{+370}_{-400}	$8.21^{+0.08}_{-0.08}$	$1.34^{+0.17}_{-0.09}$	⋯
3389371380055187968	3389371384349749376	3084	29.3	6520^{+130}_{-140}	$8.14^{+0.05}_{-0.05}$	$3.03^{+0.50}_{-0.22}$	DA (2)
3400087667066875648	3400087873225289728	3560	34.2	$12,680^{+380}_{-370}$	$8.12^{+0.04}_{-0.04}$	$0.98^{+0.20}_{-0.09}$	DA (2)
3413008990266533376	3413009093345760768	3387	70.4	6520^{+140}_{-160}	$8.16^{+0.06}_{-0.06}$	$3.10^{+0.41}_{-0.25}$	DA (2)
3423222461152705536	3423222559935120000	4007	17.7	9580^{+160}_{-160}	$8.74^{+0.04}_{-0.04}$	$1.76^{+0.06}_{-0.06}$	DC (2)
3435597013551204736	3435597013551206784	3289	10.7	7180^{+290}_{-290}	$8.25^{+0.09}_{-0.08}$	$2.73^{+0.28}_{-0.25}$	⋯
3630646463602449664	3630648387747801088	3398	21.9	$12,230^{+150}_{-150}$	$8.57^{+0.04}_{-0.04}$	$1.02^{+0.02}_{-0.01}$	DA (2)
3724362340763265536	3724362336470991488	3066	24.9	7930^{+100}_{-110}	$8.26^{+0.04}_{-0.04}$	$2.08^{+0.27}_{-0.09}$	DQ (10)
3726944921778222080	3726944951843168768	3464	37.1	$10,480^{+140}_{-140}$	$8.13^{+0.04}_{-0.04}$	$1.25^{+0.13}_{-0.07}$	DA (2)
3727701042180797952	3727701007821059072	3247	40.0	8500^{+160}_{-170}	$8.28^{+0.05}_{-0.05}$	$1.84^{+0.32}_{-0.12}$	DQ (4)
3733304978070296320	3733305179932909312	3098	173.7	5810^{+70}_{-70}	$8.21^{+0.04}_{-0.04}$	$4.73^{+0.11}_{-0.11}$	DA (6)
3805246023875111680	3805246019580616960	3946	20.4	$12,204^{+680}_{-790}$	$8.46^{+0.08}_{-0.07}$	$0.94^{+0.07}_{-0.07}$	⋯
3831257784633494016	3831257823288140544	3306	37.9	9680^{+160}_{-180}	$8.33^{+0.04}_{-0.04}$	$1.42^{+0.03}_{-0.03}$	DA (5)
3839256319408219008	3839256319408293248	5565	12.5	7980^{+200}_{-200}	$8.19^{+0.06}_{-0.06}$	$1.94^{+0.18}_{-0.10}$	⋯
3870805121940366720	3870804537824812800	3471	129.3	$10,160^{+420}_{-450}$	$8.22^{+0.09}_{-0.08}$	$1.22^{+0.17}_{-0.09}$	⋯

Table 1
(Continued)

MS Gaia DR3 ID	WD Gaia DR3 ID	MS $T_{\rm eff}$ (K)	MS $P_{\rm rot}$ (days)	WD $T_{\rm eff}$ (K)	WD log(g) (dex)	WD Total Age (Gyr)	WD Spectral Type
3897698321657960832	3897698317362400384	3574	24.0	$12,010^{+390}_{-450}$	$8.52^{+0.05}_{-0.05}$	$1.00^{+0.05}_{-0.03}$	…
3907622513610306432	3907622479250567808	3406	57.0	6950^{+80}_{-90}	$8.19^{+0.04}_{-0.04}$	$2.66^{+0.10}_{-0.12}$	DA (2)
3919287679146000640	3919287674850641792	5249	14.6	$10,710^{+310}_{-350}$	$8.29^{+0.05}_{-0.05}$	$1.12^{+0.06}_{-0.03}$	…
3931756484602030976	3931756484602030848	3294	100.1	7150^{+90}_{-90}	$8.21^{+0.04}_{-0.04}$	$2.67^{+0.51}_{-0.20}$	DQ (6)
3944167939359417088	3944167939360964480	3608	13.0	$12,480^{+890}_{-980}$	$8.33^{+0.10}_{-0.08}$	$0.86^{+0.08}_{-0.07}$	…
3956995877097644416	3956995666643307008	4276	43.5	$10,700^{+440}_{-480}$	$8.39^{+0.07}_{-0.07}$	$1.20^{+0.04}_{-0.07}$	…
4283721804641828480	4283721800317089920	3326	138.5	6790^{+100}_{-100}	$8.34^{+0.04}_{-0.04}$	$3.75^{+0.09}_{-0.07}$	DA (2)
4310991582806231296	4310991685885480064	3343	126.7	8910^{+170}_{-180}	$8.17^{+0.04}_{-0.04}$	$1.57^{+0.13}_{-0.08}$	DA (2)
4371782034475387776	4371782030179914624	3304	26.3	6100^{+70}_{-80}	$8.14^{+0.04}_{-0.04}$	$3.67^{+0.32}_{-0.22}$	DA (2)
4433378806164302464	4433378806161595904	3394	36.7	5500^{+70}_{-70}	$8.10^{+0.04}_{-0.04}$	$5.19^{+1.12}_{-0.37}$	DA (2)
4447660805076826880	4447663760014329344	3383	54.5	9660^{+450}_{-500}	$8.34^{+0.10}_{-0.09}$	$1.43^{+0.09}_{-0.07}$	…
4465117102652542336	4465117098356736000	3676	39.1	6460^{+90}_{-100}	$8.15^{+0.04}_{-0.04}$	$3.14^{+0.27}_{-0.18}$	…
4517946196857223808	4517946192529261824	4810	17.9	8450^{+510}_{-590}	$8.40^{+0.13}_{-0.13}$	$2.29^{+0.27}_{-0.23}$	…
4563562151123622656	4563562426001533696	3461	54.6	7340^{+110}_{-120}	$8.20^{+0.04}_{-0.04}$	$2.35^{+0.11}_{-0.09}$	…
4565593739374133504	4565593735079515904	3232	178.0	6440^{+110}_{-120}	$8.30^{+0.05}_{-0.05}$	$4.06^{+0.16}_{-0.15}$	…
4565737053842898304	4565737049547212544	3718	32.5	8730^{+280}_{-300}	$8.31^{+0.08}_{-0.07}$	$1.75^{+0.09}_{-0.11}$	…
4611559819405628672	4611559815111559552	3532	33.7	8740^{+250}_{-280}	$8.23^{+0.07}_{-0.07}$	$1.64^{+0.14}_{-0.09}$	…
6222883046075139968	6222882251504782720	3271	274.2	$15,330^{+290}_{-300}$	$8.38^{+0.04}_{-0.04}$	$0.61^{+0.01}_{-0.02}$	DA (2)
6236729088627705216	6236729329145889792	5437	26.0	5290^{+80}_{-80}	$8.18^{+0.05}_{-0.05}$	$6.78^{+0.22}_{-0.15}$	DA (2)
720018767158643072	720018767158642944	3782	43.3	$12,830^{+690}_{-780}$	$8.27^{+0.06}_{-0.06}$	$0.81^{+0.08}_{-0.05}$	DC+dM (5)

Notes. In the last column, we report the spectral type of the WDs, when available, and their references in brackets.
References. WD spectral types have been obtained from (1) B. Zuckerman et al. (2003); (2) Gaia XP spectra (O. Vincent et al. 2024); (3) D. J. Eisenstein et al. (2006); (4) S. O. Kepler et al. (2015); (5) S. J. Kleinman et al. (2013b); (6) A. Caron et al. (2023); (7) F. Hardy et al. (2023); (8) G. P. McCook & E. M. Sion (1999); (9) S. O. Kepler et al. (2016); (10) S. Coutu et al. (2019); (11) M. M. Limoges et al. (2015). A colon after spectral types denote uncertain spectral classification.

(This table is available in machine-readable form in the online article.)

Appendix C
Rotational Isochrones

Selected rotational isochrones calculated with our models are reported in Table 2. The table lists the surface rotation period, in days, as a function of stellar mass and age; effective temperatures are also given, as computed from a 2.0 Gyr gyrochrone.

Table 2
Rotational Isochrones Constructed Using a Solar-metallicity, $f_{\rm spots} = 0\%$ Model Grid

M ($M_\odot$)	$T_{\rm eff}$ (K)	Ages (Gyr)										
		0.5	1.0	2.0	3.0	4.0	5.0	6.0	7.0	8.0	9.0	10.0
0.18	3200	0.75	2.78	32.46	53.27	68.01	80.12	90.67	100.14	108.84	116.93	124.53
0.19	3221	0.84	3.19	35.8	56.42	71.35	83.7	94.5	104.24	113.19	121.52	129.35
0.20	3241	0.94	3.66	39.07	59.66	74.83	87.47	98.57	108.59	117.8	126.4	134.48
0.21	3259	1.04	4.18	42.32	63.03	78.51	91.48	102.9	113.22	122.73	131.59	139.91
0.22	3276	1.16	4.77	45.63	66.58	82.44	95.78	107.55	118.2	128.0	137.13	145.71
0.23	3292	1.29	5.4	49.0	70.34	86.65	100.42	112.56	123.55	133.66	143.07	151.9
0.24	3307	1.42	6.1	52.56	74.43	91.26	105.49	118.04	129.4	139.83	149.52	158.61
0.25	3321	1.56	6.84	56.34	78.9	96.34	111.09	124.08	135.82	146.58	156.58	165.93
0.26	3335	1.69	7.08	57.58	81.81	100.31	115.83	129.44	141.68	152.88	163.25	172.95
0.27	3348	1.72	6.57	57.95	84.48	104.3	120.75	135.08	147.91	159.61	170.41	180.49
0.28	3360	1.85	7.14	62.79	90.81	111.63	128.84	143.77	157.1	169.23	180.42	190.85
0.29	3372	2.0	7.45	66.35	96.98	119.27	137.5	153.21	167.18	179.85	191.52	202.37
0.30	3383	2.12	8.03	73.43	106.78	130.58	149.84	166.34	180.95	194.17	206.32	217.61
0.31	3394	2.3	8.85	84.02	121.16	146.81	167.25	184.62	199.92	213.73	226.4	238.15
0.32	3405	2.49	9.74	102.15	145.87	173.89	195.64	213.9	229.89	244.27	257.42	269.61
0.33	3416	2.7	10.92	57.15	161.66	199.83	225.93	246.77	264.56	280.3	294.56	307.7
0.34	3426	2.94	11.15	43.67	57.95	104.08	188.55	227.14	254.86	277.38	296.76	314.01
0.35	3437	3.05	12.33	43.15	57.87	67.56	76.75	85.68	94.08	102.01	116.45	194.68

Table 2
(Continued)

M ($M_{\odot}$)	$T_{\rm eff}$ (K)	Ages (Gyr) 0.5	1.0	2.0	3.0	4.0	5.0	6.0	7.0	8.0	9.0	10.0
0.36	3446	3.19	10.99	30.03	43.71	55.65	64.93	72.68	79.42	84.58	89.38	94.24
0.37	3458	3.61	13.4	30.65	43.47	53.35	61.13	65.2	70.98	76.22	80.69	84.59
0.38	3470	4.1	15.24	30.85	42.64	50.44	54.57	60.82	66.18	70.58	74.34	77.44
0.39	3484	4.69	16.46	30.94	40.87	45.81	51.97	57.81	62.34	66.05	68.99	71.47
0.40	3497	5.38	17.33	30.89	38.59	43.83	50.25	55.22	59.04	62.01	64.26	66.11
0.41	3512	6.24	18.31	30.89	37.09	43.2	48.97	53.17	56.29	58.64	60.43	61.73
0.42	3526	7.27	18.88	30.31	36.05	42.16	47.17	50.61	53.05	54.81	56.11	57.02
0.43	3542	8.53	19.38	29.55	35.44	41.04	45.25	48.0	49.86	51.14	52.0	52.71
0.44	3558	9.96	19.81	28.8	34.85	39.74	43.21	45.33	46.7	47.64	48.24	48.77
0.45	3575	11.05	20.15	28.28	34.09	38.33	41.11	42.71	43.72	44.41	44.86	45.3
0.46	3592	11.9	20.41	27.93	33.21	36.83	38.95	40.13	40.88	41.43	41.87	42.2
0.47	3611	12.57	20.53	27.57	32.25	35.21	36.89	37.77	38.36	38.82	39.22	39.55
0.48	3631	13.14	20.49	27.17	31.17	33.6	34.83	35.52	36.03	36.47	36.88	37.22
0.49	3651	13.42	20.15	26.38	29.79	31.68	32.64	33.21	33.67	34.04	34.47	34.9
0.50	3673	13.96	20.1	25.93	28.75	30.24	31.06	31.58	32.04	32.49	32.89	33.36
0.51	3697	14.32	19.89	25.21	27.54	28.77	29.45	29.95	30.43	30.91	31.34	31.85
0.52	3721	14.66	19.8	24.55	26.53	27.52	28.15	28.67	29.19	29.71	30.19	30.74
0.53	3747	14.84	19.62	23.78	25.36	26.24	26.85	27.4	27.96	28.52	29.06	29.65
0.54	3774	14.88	19.28	22.75	24.08	24.9	25.49	26.07	26.68	27.29	27.92	28.51
0.55	3803	14.96	19.05	22.0	23.19	23.97	24.6	25.24	25.9	26.57	27.25	27.92
0.56	3834	14.93	18.7	21.22	22.29	23.04	23.75	24.45	25.11	25.86	26.62	27.39
0.57	3866	14.78	18.25	20.34	21.34	22.13	22.89	23.65	24.43	25.23	26.02	26.88
0.58	3900	14.66	17.75	19.56	20.53	21.37	22.19	23.01	23.87	24.75	25.62	26.57
0.59	3935	14.66	17.44	19.04	20.03	20.91	21.82	22.74	23.69	24.67	25.65	26.72
0.60	3972	14.42	16.74	18.22	19.23	20.17	21.14	22.14	23.18	24.26	25.34	26.53
0.65	4164	12.97	14.08	15.45	16.79	18.23	19.75	21.36	23.02	24.83	26.79	28.76
0.70	4395	10.93	11.9	13.76	15.8	18.04	20.49	23.14	25.95	28.9	31.92	35.08
0.75	4638	9.21	10.43	13.12	16.19	19.58	23.17	26.91	30.7	34.44	38.2	41.89
0.80	4885	7.97	9.62	13.44	17.73	22.15	26.51	30.77	34.9	38.91	42.82	46.65
0.85	5124	7.28	9.51	14.57	19.72	24.64	29.23	33.63	37.84	42.03	46.16	50.4
0.90	5347	6.89	9.76	15.74	21.25	26.27	30.93	35.46	39.93	44.47	49.21	54.33
0.95	5554	6.76	10.15	16.55	22.08	27.09	31.87	36.64	41.56	46.89	53.11	***
1.00	5742	6.68	10.34	16.72	22.13	27.12	32.03	37.22	43.17	***	***	***
1.05	5912	6.62	10.23	16.23	21.33	26.2	31.37	***	***	***	***	***
1.10	6067	6.19	9.42	14.71	19.3	24.08	***	***	***	***	***	***
1.15	6206	5.38	7.97	12.27	16.33	21.77	***	***	***	***	***	***

Notes. Models corresponding to masses greater than 0.6 $M_{\odot}$ are core-envelope decoupling models whose cores are rotating too fast, and therefore the surface rotation periods reported here are an underestimate. Missing entries in a gyrochrone (indicated with "***") correspond to stars that have already left the main sequence by that age and that have surpassed the critical Rossby number ($Ro_{crit} = 2.08$; J. L. van Saders et al. 2019).

(This table is available in machine-readable form in the online article.)

ORCID iDs

Federica Chiti https://orcid.org/0000-0001-5180-2271
Jennifer L. van Saders https://orcid.org/0000-0002-4284-8638
Tyler M. Heintz https://orcid.org/0000-0003-3868-1123
J. J. Hermes https://orcid.org/0000-0001-5941-2286
J. M. Joel Ong (王加冕) https://orcid.org/0000-0001-7664-648X
Daniel R. Hey https://orcid.org/0000-0003-3244-5357

References

Abazajian, K., Adelman-McCarthy, J. K., Agüeros, M. A., et al. 2004, AJ, 128, 502
Abdurro'uf, Accetta, K., Aerts, C., et al. 2022, ApJS, 259, 35
Adelberger, E. G., Garcia, A., Robertson, R. G. H., et al. 2011, RvMP, 83, 195
Allard, F., Hauschildt, P. H., Alexander, D. R., & Starrfield, S. 1997, ARA&A, 35, 137
Amard, L., & Matt, S. P. 2020, ApJ, 889, 108
Amard, L., Palacios, A., Charbonnel, C., et al. 2019, A&A, 631, A77
Bahcall, J. N., & Pinsonneault, M. H. 1992, RvMP, 64, 885
Bahcall, J. N., Pinsonneault, M. H., & Wasserburg, G. J. 1995, RvMP, 67, 781
Barnes, S. A. 2007, ApJ, 669, 1167
Barnes, S. A., & Kim, Y.-C. 2010, ApJ, 721, 675
Basu, S., & Antia, H. M. 1995, MNRAS, 276, 1402
Bédard, A., Bergeron, P., Brassard, P., & Fontaine, G. 2020, ApJ, 901, 93
Bergeron, P., Dufour, P., Fontaine, G., et al. 2019, ApJ, 876, 67
Bergeron, P., Wesemael, F., & Beauchamp, A. 1995, PASP, 107, 1047
Böhm-Vitense, E. 1958, ZAp, 46, 108
Boudreaux, E. M., Garcia Soto, A., & Chaboyer, B. C. 2024, ApJ, 965, 56
Buder, S., Asplund, M., Duong, L., et al. 2018, MNRAS, 478, 4513
Cao, L., & Pinsonneault, M. H. 2022, MNRAS, 517, 2165
Cao, L., Pinsonneault, M. H., & van Saders, J. L. 2023, ApJL, 951, L49
Caron, A., Bergeron, P., Blouin, S., & Leggett, S. K. 2023, MNRAS, 519, 4529
Chabrier, G. 2003, PASP, 115, 763

Chaplin, W. J., Kjeldsen, H., Bedding, T. R., et al. 2011, ApJ, 732, 54
Chen, X., Wang, S., Deng, L., et al. 2020, ApJS, 249, 18
Claytor, Z. R., van Saders, J. L., Cao, L., et al. 2024, ApJ, 962, 47
Claytor, Z. R., van Saders, J. L., Santos, Â. R. G., et al. 2020, ApJ, 888, 43
Coutu, S., Dufour, P., Bergeron, P., et al. 2019, ApJ, 885, 74
Cox, J. P., & Giuli, R. T. 1968, Principles of Stellar Structure (New York: Gordon and Breach)
Cukanovaite, E., Tremblay, P.-E., Bergeron, P., et al. 2021, MNRAS, 501, 5274
Cummings, J. D., Kalirai, J. S., Choi, J., et al. 2019, ApJL, 871, L18
Cummings, J. D., Kalirai, J. S., Tremblay, P. E., & Ramirez-Ruiz, E. 2015, ApJ, 807, 90
Cummings, J. D., Kalirai, J. S., Tremblay, P. E., & Ramirez-Ruiz, E. 2016, ApJ, 818, 84
Cummings, J. D., Kalirai, J. S., Tremblay, P. E., Ramirez-Ruiz, E., & Choi, J. 2018, ApJ, 866, 21
Curtis, J. L., Agüeros, M. A., Douglas, S. T., & Meibom, S. 2019, ApJ, 879, 49
Curtis, J. L., Agüeros, M. A., Matt, S. P., et al. 2020, ApJ, 904, 140
Denissenkov, P. A., Pinsonneault, M., Terndrup, D. M., & Newsham, G. 2010, ApJ, 716, 1269
Díez Alonso, E., Caballero, J. A., Montes, D., et al. 2019, A&A, 621, A126
Donati, J.-F., Morin, J., Petit, P., et al. 2008, MNRAS, 390, 545
D'Orazi, V., Oliva, E., Bragaglia, A., et al. 2020, A&A, 633, A38
Douglas, S. T., Agüeros, M. A., Covey, K. R., & Kraus, A. 2017, ApJ, 842, 83
Douglas, S. T., Curtis, J. L., Agüeros, M. A., et al. 2019, ApJ, 879, 100
Dungee, R., van Saders, J., Gaidos, E., et al. 2022, ApJ, 938, 118
Eisenstein, D. J., Liebert, J., Harris, H. C., et al. 2006, ApJS, 167, 40
El-Badry, K., & Rix, H.-W. 2018, MNRAS, 480, 4884
El-Badry, K., Rix, H.-W., & Heintz, T. M. 2021, MNRAS, 506, 2269
Epstein, C. R., & Pinsonneault, M. H. 2014, ApJ, 780, 159
Feiden, G. A., Skidmore, K., & Jao, W.-C. 2021, ApJ, 907, 53
Ferguson, J. W., Alexander, D. R., Allard, F., et al. 2005, ApJ, 623, 585
Fields, C. E., Farmer, R., Petermann, I., Iliadis, C., & Timmes, F. X. 2016, ApJ, 823, 46
Fontaine, G., Brassard, P., & Bergeron, P. 2001, PASP, 113, 409
Foreman-Mackey, D., Hogg, D. W., Lang, D., & Goodman, J. 2013, PASP, 125, 306
France, K., Arulanantham, N., Fossati, L., et al. 2018, ApJS, 239, 16
Gaia Collaboration 2022, yCat, 1358, 0
García-Berro, E., & Oswalt, T. D. 2016, NewAR, 72, 1
García-Berro, E., Torres, S., Althaus, L. G., et al. 2010, Natur, 465, 194
Gentile Fusillo, N. P., Tremblay, P. E., Cukanovaite, E., et al. 2021, MNRAS, 508, 3877
Giammichele, N., Bergeron, P., & Dufour, P. 2012, ApJS, 199, 29
Grevesse, N., & Sauval, A. J. 1998, SSRv, 85, 161
Hall, O. J., Davies, G. R., van Saders, J., et al. 2021, NatAs, 5, 707
Hansen, B. M. S., Kalirai, J. S., Anderson, J., et al. 2013, Natur, 500, 51
Hardy, F., Dufour, P., & Jordan, S. 2023, MNRAS, 520, 6111
Hartman, J. D., Bakos, G. Á, Kovacs, G., & Noyes, R. W. 2010, MNRAS, 408, 475
Heintz, T. M., Hermes, J. J., El-Badry, K., et al. 2022, ApJ, 934, 148
Heintz, T. M., Hermes, J. J., Tremblay, P. E., et al. 2024, ApJ, 969, 68
Heinze, A. N., Tonry, J. L., Denneau, L., et al. 2018, AJ, 156, 241
Holberg, J. B., Oswalt, T. D., Sion, E. M., Barstow, M. A., & Burleigh, M. R. 2013, MNRAS, 435, 2077
Iglesias, C. A., & Rogers, F. J. 1996, ApJ, 464, 943
Janes, K., Barnes, S. A., Meibom, S., & Hoq, S. 2013, AJ, 145, 7
Jao, W.-C., Henry, T. J., Gies, D. R., & Hambly, N. C. 2018, ApJL, 861, L11
Jao, W.-C., Henry, T. J., White, R. J., et al. 2023, AJ, 166, 63
Jayasinghe, T., Kochanek, C. S., Stanek, K. Z., et al. 2018, MNRAS, 477, 3145
Jeffery, E. J., von Hippel, T., DeGennaro, S., et al. 2011, ApJ, 730, 35
Kawaler, S. D. 1988, ApJ, 333, 236
Kepler, S. O., Pelisoli, I., Koester, D., et al. 2015, MNRAS, 446, 4078
Kepler, S. O., Pelisoli, I., Koester, D., et al. 2016, MNRAS, 455, 3413
Kim, Y.-C., & Demarque, P. 1996, ApJ, 457, 340
Kleinman, S. J., Kepler, S. O., Koester, D., et al. 2013a, ApJS, 204, 5
Kleinman, S. J., Kepler, S. O., Koester, D., et al. 2013b, ApJS, 204, 5
Koester, D. 2010, MmSAI, 81, 921
Kollmeier, J. A., Zasowski, G., Rix, H.-W., et al. 2017, arXiv:1711.03234
Lallement, R., Vergely, J. L., Babusiaux, C., & Cox, N. L. J. 2022, A&A, 661, A147
Lanzafame, A. C., & Spada, F. 2015, A&A, 584, A30
Liebert, J., Bergeron, P., & Holberg, J. B. 2005, ApJS, 156, 47
Limoges, M. M., Bergeron, P., & Lépine, S. 2015, ApJS, 219, 19
Lu, Y., Angus, R., Foreman-Mackey, D., & Hattori, S. 2024a, AJ, 167, 159
Lu, Y., See, V., Amard, L., Angus, R., & Matt, S. P. 2024b, NatAs, 8, 223
Lu, Y. L., Angus, R., Curtis, J. L., David, T. J., & Kiman, R. 2021, AJ, 161, 189
Lu, Y. L., Curtis, J. L., Angus, R., David, T. J., & Hattori, S. 2022, AJ, 164, 251
MacGregor, K. B., & Brenner, M. 1991, ApJ, 376, 204
Mann, A. W., Feiden, G. A., Gaidos, E., Boyajian, T., & von Braun, K. 2015, ApJ, 804, 64
Matt, S. P., MacGregor, K. B., Pinsonneault, M. H., & Greene, T. P. 2012, ApJL, 754, L26
McCook, G. P., & Sion, E. M. 1999, ApJS, 121, 1
McQuillan, A., Aigrain, S., & Mazeh, T. 2013, MNRAS, 432, 1203
McQuillan, A., Mazeh, T., & Aigrain, S. 2014a, ApJS, 211, 24
McQuillan, A., Mazeh, T., & Aigrain, S. 2014b, yCat, J/ApJS/211/24
Meibom, S., Barnes, S. A., Platais, I., et al. 2015, Natur, 517, 589
Meibom, S., Barnes, S. A., Latham, D. W., et al. 2011, ApJL, 733, L9
Mier, P. R. 2017, pablormier/yabox: v1.0.3, v1.0.3, Zenodo, doi:10.5281/zenodo.848679
Morgan, D. P., West, A. A., Garcés, A., et al. 2012, AJ, 144, 93
Newton, E. R., Irwin, J., Charbonneau, D., et al. 2017, ApJ, 834, 85
Newton, E. R., Irwin, J., Charbonneau, D., et al. 2016, yCat, J/ApJ/821/93
Newton, E. R., Mondrik, N., Irwin, J., Winters, J. G., & Charbonneau, D. 2018, AJ, 156, 217
Oelkers, R. J., Rodriguez, J. E., Stassun, K. G., et al. 2018, AJ, 155, 39
Paxton, B., Bildsten, L., Dotter, A., et al. 2011, ApJS, 192, 3
Paxton, B., Cantiello, M., Arras, P., et al. 2013, ApJS, 208, 4
Paxton, B., Marchant, P., Schwab, J., et al. 2015, ApJS, 220, 15
Pinsonneault, M. H., Kawaler, S. D., Sofia, S., & Demarque, P. 1989, ApJ, 338, 424
Pizzolato, N., Maggio, A., Micela, G., Sciortino, S., & Ventura, P. 2003, A&A, 397, 147
Raddi, R., Torres, S., Rebassa-Mansergas, A., et al. 2022, A&A, 658, A22
Rebassa-Mansergas, A., Schreiber, M. R., & Gänsicke, B. T. 2013, MNRAS, 429, 3570
Rebassa-Mansergas, A., Anguiano, B., García-Berro, E., et al. 2016, MNRAS, 463, 1137
Rebassa-Mansergas, A., Maldonado, J., Raddi, R., et al. 2021, MNRAS, 505, 3165
Rebassa-Mansergas, A., Maldonado, J., Raddi, R., et al. 2023, MNRAS, 526, 4787
Rebull, L. M., Stauffer, J. R., Cody, A. M., et al. 2018, AJ, 155, 196
Rebull, L. M., Stauffer, J. R., Bouvier, J., et al. 2016, AJ, 152, 113
Recio-Blanco, A., de Laverny, P., Palicio, P. A., et al. 2023, A&A, 674, A29
Reiners, A., & Basri, G. 2009, A&A, 496, 787
Reinhold, T., & Hekker, S. 2020, A&A, 635, A43
Riello, M., De Angeli, F., Evans, D. W., et al. 2021, A&A, 649, A3
Rogers, F. J., & Nayfonov, A. 2002, ApJ, 576, 1064
Rogers, F. J., Swenson, F. J., & Iglesias, C. A. 1996, ApJ, 456, 902
Salpeter, E. E. 1954, AuJPh, 7, 373
Santos, A. R. G., Breton, S. N., Mathur, S., & Garcia, R. A. 2021, yCat, J/ApJS/255/17
Santos, A. R. G., García, R. A., Mathur, S., et al. 2019, ApJS, 244, 21
Santos, A. R. G., Garcia, R. A., Mathur, S., et al. 2020, yCat, J/ApJS/244/21
Schou, J., Antia, H. M., Basu, S., et al. 1998, ApJ, 505, 390
Shappee, B. J., Prieto, J. L., Grupe, D., et al. 2014, ApJ, 788, 48
Silva Aguirre, V., Bojsen-Hansen, M., Slumstrup, D., et al. 2018, MNRAS, 475, 5487
Simonian, G. V. A., Pinsonneault, M. H., & Terndrup, D. M. 2019, ApJ, 871, 174
Skinner, J. N., Morgan, D. P., West, A. A., Lépine, S., & Thorstensen, J. R. 2017, AJ, 154, 118
Skumanich, A. 1972, ApJ, 171, 565
Soderblom, D. R. 2010, ARA&A, 48, 581
Somers, G., Cao, L., & Pinsonneault, M. H. 2020, ApJ, 891, 29
Somers, G., & Pinsonneault, M. H. 2015, ApJ, 807, 174
Somers, G., & Pinsonneault, M. H. 2016, ApJ, 829, 32
Somers, G., Stauffer, J., Rebull, L., Cody, A. M., & Pinsonneault, M. 2017, ApJ, 850, 134
Spada, F., & Lanzafame, A. C. 2020, A&A, 636, A76
Spergel, D., Gehrels, N., Baltay, C., et al. 2015, arXiv:1503.03757
Spitzer, L. J., & Schwarzschild, M. 1951, ApJ, 114, 385
Takeda, Y., Hashimoto, O., & Honda, S. 2017, PASJ, 69, 1
Temmink, K. D., Toonen, S., Zapartas, E., Justham, S., & Gänsicke, B. T. 2020, A&A, 636, A31
Thoul, A. A., Bahcall, J. N., & Loeb, A. 1994, ApJ, 421, 828
van Saders, J. L., Ceillier, T., Metcalfe, T. S., et al. 2016, Natur, 529, 181
van Saders, J. L., & Pinsonneault, M. H. 2012a, ApJ, 751, 98
van Saders, J. L., & Pinsonneault, M. H. 2012b, ApJ, 746, 16

van Saders, J. L., & Pinsonneault, M. H. 2013, ApJ, 776, 67
van Saders, J. L., Pinsonneault, M. H., & Barbieri, M. 2019, ApJ, 872, 128
Vincent, O., Barstow, M. A., Jordan, S., et al. 2024, A&A, 682, A5
Vitense, E. 1953, ZAp, 32, 135
White, R. J., & Ghez, A. M. 2001, ApJ, 556, 265
Wielen, R. 1971, A&A, 13, 309
Willems, B., & Kolb, U. 2004, A&A, 419, 1057
Williams, J. P., & Cieza, L. A. 2011, ARA&A, 49, 67
Winget, D. E., Kepler, S. O., Campos, F., et al. 2009, ApJL, 693, L6
Wood, B. E., Redfield, S., Linsky, J. L., Müller, H.-R., & Zank, G. P. 2005, ApJS, 159, 118
Wright, N. J., Drake, J. J., Mamajek, E. E., & Henry, G.W. 2011, ApJ, 743, 16
Wright, N. J., Newton, E. R., Williams, P. K. G., Drake, J. J., & Yadav, R. K. 2018, MNRAS, 479, 2351
Zhao, J. K., Oswalt, T. D., Rudkin, M., Zhao, G., & Chen, Y. Q. 2011, AJ, 141, 107
Zhong, J., Li, J., Carlin, J. L., et al. 2020, yCat, J/ApJS/244/8
Zuckerman, B., Koester, D., Reid, I. N., & Hünsch, M. 2003, ApJ, 596, 477